Universitat
de les Illes Balears

FINAL DEGREE PROJECT

FINITE TEMPERATURE EFFECTS ON DIPOLAR SUPERFLUIDS

Bartolomé Mestre Fons

Degree in Physics

Faculty of Sciences

Academic year 2022-23

FINITE TEMPERATURE EFFECTS ON DIPOLAR SUPERFLUIDS

Bartolomé Mestre Fons

Final Degree Project

Faculty of Sciences

University of the Balearic Islands

Academic Year 2022-23

Key words:

Bose-Einstein condensates, Gross-Pitaevskii equation, Local density approximation, Hartree-Fock-Bogoliubov Theory, superfluid-supersolid phase-transition.

Thesis Supervisor's Name: Fabian Maucher

Abstract

In the present work we discuss the dependency of the phase-transition between a superfluid and a supersolid of a dipolar Bose-Einstein condensate confined to a tubular geometry on temperature employing beyond mean-field corrections. For that matter we consider quantum as well as thermal fluctuations. We employ a simplified variational approximation in order to obtain the energy functional which yields phase diagrams approximately. Qualitatively consistent with [28, 30], we find that one might expect melting into a crystal or supersolid.

Abstract

En el presente trabajo discutimos la dependencia de la transición de fase entre superfluido y supersólido de un condensado de Bose-Einstein dipolar con la temperatura en una geometría cilíndrica bajo correccions más allá del campo medio. Para ello, se introducen fluctuaciones cuánticas junto a correcciones térmicas. Utilizamos una aproximación variacional simplificada con el fin de obtener el funcional de energía que posibilita estudiar el diagrama de fase. Cualitativamente de acuerdo con [28, 30], un aumento de la temperatura conduce a una cristalización del sistema o a un supersólido.

Abstract

En el present treball discutim la dependència de la transició de fase entre superfluid i supersòlid d'un condensat de Bose-Einstein dipolar amb la temperatura dins una geometria cilíndrica amb correccions més enllà del camp mitjà. Per a aquest fi, introduim fluctuacions quàntiques juntament amb correccions tèrmiques. Empram una aproximació variacional simplificada per obtenir el funcional d'energia que possibilita estudiar el diagrama de fase. Qualitativament d'acord amb [28, 30], es troba que un augment en la temperatura condueix a la cristalització del sistema o a un supersòlid.

Index

Chapter 1

Introduction

1.1 Historical Background

The prediction of Bose-Einstein condensation (BEC) in 1924 is attributed to Satyendra Nath Bose and Albert Einstein [29][1]. They discussed the *Bose gas*[1] from a quantum-statistical framework.

When cooling an N-particle dilute system, the wave-nature of particles becomes relevant, as expressed by the thermal de Broglie wavelength λ_{dB} which scales like $\lambda_{\mathrm{dB}} \propto \frac{1}{\sqrt{T}}$. Therefore, upon cooling to sufficiently low temperature such that the mean particle distance becomes comparable to the de Broglie wavelength, matter-wave start overlapping and forming a coherent single matter-wave. The situation is sketched in Fig. 1.1. *Pauli's exclusion principle*[2] does not inhibit populating the ground state, as we consider Bosons (with integer spin number).

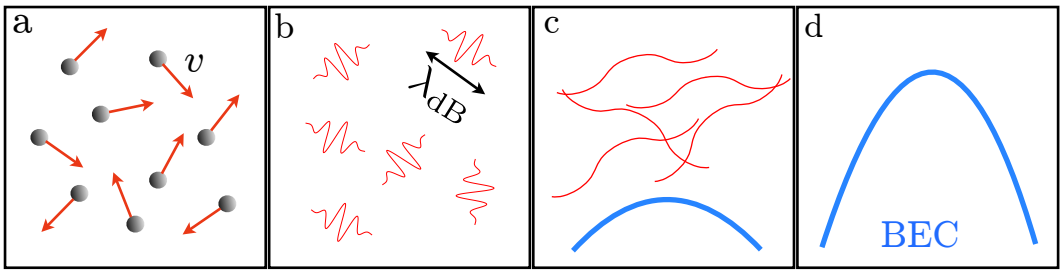

Figure 1.1: The basic idea of condensation. (a) At high temperatures the atoms behave completely particle-like, akin to billiard balls. (b) Upon lowering temperature, the wave-nature becomes more appreciable and the particles more delocalised. (c) When reaching the critical temperature T_{cr}, where the mean particle distance becomes comparable to the de Broglie wavelength, the associated matter-waves start overlapping and subsequently Bose-Einstein condensation occurs. (d) At a sufficiently low temperature ($T < T_{\mathrm{cr}}$), the atoms loose their individual identity and form a single coherent giant matter wave. It is an exciting phenomenon, as it permits to see the quantum wave function on a macroscopic scale with your bare eye. Source: adapted from [17, 32].

Wieman, Ketterle and Cornell were awarded the Nobel Prize in 2001 for "for the achievement of Bose-Einstein condensation in dilute gases of alkali atoms". Since then, Bose-Einstein condensation has been realised in other species of atoms (chromium in 2005 [11], dysprosium in 2011 [23] and erbium in 2012 [2]).

[1] A gas made of particles which possess integer spin (e.g. photons) or a composite particle containing an even number of fermions (which the latter possesses half-odd-integer spin).

[2] Fermions (e.g. electrons) cannot share the same quantum state due to this principle.

The delay between the theoretical prediction in 1924 and its realisation was due to the inherent difficulty to reach the extremely low temperatures required to realise this new form of matter. Laser cooling and evaporative cooling represent essential experimental advances that rendered the observation of Bose-Einstein condensation possible. Claude Cohen-Tannoudji, Steven Chu, and William Daniel Phillips were awarded the Nobel Prize "for development of methods to cool and trap atoms with laser light" in 1997.

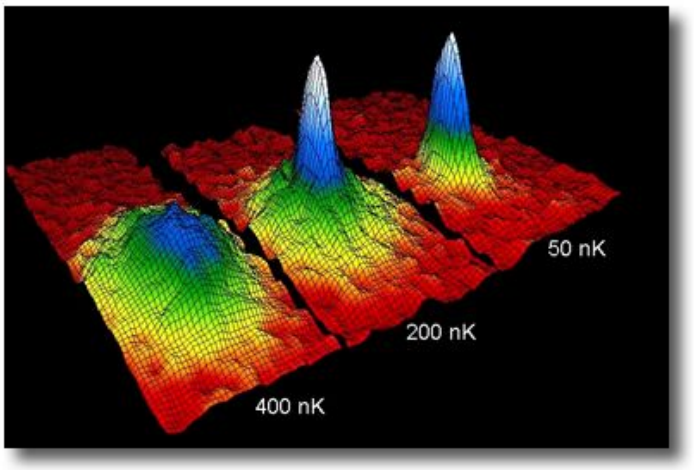

Figure 1.2: Velocity distribution for three different temperatures (400 nK, 200 nK, 50 nK) for a gas of ^{87}Rb atoms, confirming the discovery of a new state of matter, a Bose-Einstein condensate, by researchers from NIST/JILA/CU-Boulder. The initial figure at 400 nK shows a thermal distribution that upon further cooling qualitatively changes its shape indicating the formation of a BEC. Source: [9]

BEC offers a unique window to visualize quantum phenomena to the macroscopic scale. Recently, practical applications on quantum computing have been developed [19] as one of the fundamental difficulties with quantum computing is that quantum states are very sensitive to their surroundings. A theoretical framework of coding information via BEC was investigated in 2012 [8] by suggestion of the implementation of two component BECs. For that matter, BECs can be put in an arbitrary superposition of two states, as qubits. Therefore, the possibility of producing quantum entanglement via BEC opens up several directions for investigating this surprising behaviour. As suggested in [7], two coherent BEC in quantum entanglement may offer an alternative to standard quantum computation beyond standard qubit schemes.

An interesting aspect of Bose-Einstein condensates is the fact that they can feature superfluidity. A superfluid is a fluid with zero viscosity, that is a complete absence of friction between the different layers. Roughly fifty years ago speculations were made whether solids can also be superfluid [21]. At first sight, that appears to be completely absurd in that we think that a solid should display shear or resistance to deformation, as the atoms usually maintain their position at the given lattice site.

Dipolar Bose-Einstein condensates were thought to not be suitable candidates for the realisation of supersolidity, as on the mean-field level collapse of the condensate is its ultimated predicted faith. However, a pioneering work in 2016 reported the observation of the Rosenzweig instability in dipolar BECs [16], which experimentally established that in fact beyond mean-field effects where at play. Later a theoretical framework to describe these beyond mean-field effects was found.

These beyond mean-field effects in fact made the realisation of supersolids in dipolar BECs possible due to a subtle interplay between inter-atomic interactions and quantum-fluctuations. In the typical description temperature is assumed to be negligible. However, a recent experimental work [30] appears to suggest another surprise: raising the temperature slightly, such that coherence still remains, can

promote the formation of a supersolid. This appears to be counter-intuitive, as heating usually leads to additional motion that should be thought to inhibit crystallisation. A recent work [28] showed that this curious behaviour can indeed be predicted by an extended model [3, 28]. In this paper we want to see whether a simple variational approximation the phase diagram leads to similar results and at least qualitatively predicts behaviour that is consistent with [30, 28].

Chapter 2

Theoretical fundamentals

In this section we first employ the mean-field approximation to obtain the Gross-Pitaevskii equation. We extend our derivations for the zero-temperature regime by introducing the Hartee-Fock-Bogoliubov formalism, where quantum fluctuations are at play. Employing the Local Density Approximation, we introduce the Lee-Huang-Yang corrections describing quantum fluctuations. These derivations yield the energy functional which captures the physics of BEC. In the Supplementary information appendix we provide further details on the mathematical derivations shown in the following chapter.

2.1 Gross-Pitaevskii equation

Here, the mean-field theory at $T = 0$ is employed to describe the N-interacting particles system. Upon the previous theoretical framework, the many-body Hammiltonian (described by the bosonic field operator $\Psi(\mathbf{r})$ in the second-quantization framework) for N interacting bosons of mass m under a confining potential $V_{\text{ext}}(\mathbf{r})$ [18] is given by

$$\hat{H}_0 = \int d^3\mathbf{r}\hat{\Psi}^\dagger(\mathbf{r})H_0(\mathbf{r})\hat{\Psi}(\mathbf{r}) + \frac{1}{2}\int\int d^3\mathbf{r}\, d^3\mathbf{r'}\hat{\Psi}^\dagger(\mathbf{r})\hat{\Psi}^\dagger(\mathbf{r'})V_{\text{int}}(\mathbf{r}-\mathbf{r'})\hat{\Psi}(\mathbf{r'})\hat{\Psi}(\mathbf{r}) \tag{2.1}$$

where H_0 is the single particle Hamiltonian $H_0 = -\frac{\hbar^2}{2m}\nabla^2 + V_{\text{ext}}(\mathbf{r})$ which accounts for the kinetic energy and the external potential. V_{int} is the two-body interaction potential (for a dilute gas, three and further-body interactions are neglected). Within the dilute gas approximation, the interaction potential is described by

$$V_{\text{int}}(\mathbf{r}) = g\left[\delta(\mathbf{r}) + \frac{3\epsilon_{dd}}{4\pi|\mathbf{r}|^3}\left(1 - 3\frac{z^2}{|\mathbf{r}|^2}\right)\right] \tag{2.2}$$

where g denotes the short-range repulsion coupling constant $g = \frac{4\pi\hbar^2 a_s}{m}$ dependent of the scattering length a_s. Experimentally, g can be manually tuned by applying external magnetic fields [24]. Moreover, $\epsilon_{dd} = \frac{a_{dd}}{a_s}$ where a_{dd} captures the dipole length. From (2.2), one finds that the interaction potential is in the form of a sum of a short-range interaction by a delta function plus a dipole-dipole long range interaction [3] (dipoles are chosen to be aligned in the y-direction). Note that a dilute Bose-gas with a condensed number of atoms N satisfies $N' - N \ll N'$ where $N'$is the total number of atoms.
In this way, the beyond mean-field approximates the field operator as a sum of a classical mean field plus fluctuations $\hat{\Psi}(\mathbf{r},t) = \langle\hat{\Psi}(\mathbf{r},t)\rangle + \hat{\Phi}(\mathbf{r},t)$ ($\langle ...\rangle$ represents the thermal average of the field operator, where it satisfies $\langle\hat{\Phi(\mathbf{r},t)}\rangle = 0$). Also, note that the first term (called $\Psi(\mathbf{r})$ from now on) is constrained to the conservation of the total number of condensed particles such that $N = \int|\Psi(\mathbf{r},t)|^2 d\mathbf{r}$. In order to obtain

the Gross-Pitaevskii equation, the Heisenberg equation $i\hbar(\partial\hat{\Psi}/\partial t) = [\hat{\Psi}, \hat{H}_0]$ applied on the field operator yields

$$i\hbar\frac{\partial}{\partial t}\hat{\Psi}(\mathbf{r},t) = \left[-\frac{\hbar^2}{2m}\nabla^2 + V_{\text{ext}}(\mathbf{r}) + \int d\mathbf{r'}\hat{\Psi}^\dagger(\mathbf{r'},t)V_{\text{int}}(\mathbf{r}-\mathbf{r'})\hat{\Psi}(\mathbf{r'},t)\right]\hat{\Psi}(\mathbf{r},t) \tag{2.3}$$

By neglecting terms of beyond zeroth order such that the operator $\hat{\Psi}(\mathbf{r},t)$ is replaced by the classical field $\Psi(\mathbf{r},t)$ upon the mean-field approximation, (2.3) yields the GP equation

$$i\hbar\frac{\partial}{\partial t}\Psi(\mathbf{r},t) = \left[-\frac{\hbar^2}{2m}\nabla^2 + V_{\text{ext}}(\mathbf{r}) + \int d\mathbf{r'}\Psi^*(\mathbf{r'},t)V_{\text{int}}(\mathbf{r}-\mathbf{r'})\Psi(\mathbf{r'},t)\right]\Psi(\mathbf{r},t) \tag{2.4}$$

From (2.4), the GP equation takes the form of a nonlinear Schrödinger equation (due to the proportionality with $|\Psi|^2$ of the last term, where if removed by setting the coupling constant g to zero we recover the Schrödinger single particle equation under a trapping potential). Note that (2.4) is modified from [18] since we include the chemical potential.
GP equation was deduced by Gross [12] and Pitaevskii [25] in 1961, and it well describes the wavefunction of a weakly interacting BEC. However, it is limited to the weakly interacting regime. In the next section, we include beyond mean-field perturbations employing the so-called Hartee-Fock-Bogoliubov formalism.

2.2 Hartee-Fock-Bogoliubov formalism

We apply the prescription of splitting the field operator by a thermal average plus a fluctuation term in (2.3) and consider the interaction potential in the most general case where short and long range dipole-dipole interactions are at play. In the stationary regime, the wavefunction is described as $\Psi(\mathbf{r}) = \Psi_0(\mathbf{r})\exp(-i\frac{\mu}{\hbar}t)$ where μ denotes the chemical potential. Therefore, the time dependence in (2.4) yields μ.

Thus it is written out in the form [3]

$$\mathcal{L}\Psi(\mathbf{r}) + \int d^3\mathbf{r'}V_{\text{int}}(\mathbf{r}-\mathbf{r'})\tilde{n}(\mathbf{r'},\mathbf{r})\Psi(\mathbf{r'}) + \int d^3\mathbf{r'}V_{\text{int}}(\mathbf{r}-\mathbf{r'})\tilde{m}(\mathbf{r'},\mathbf{r})\Psi^*(\mathbf{r'}) = 0 \tag{2.5}$$

where $\tilde{n}(\mathbf{r'},\mathbf{r}) = \langle\hat{\Phi}^\dagger(\mathbf{r'})\hat{\Phi}(\mathbf{r})\rangle$ is the non-condensed density and $\tilde{m}(\mathbf{r'},\mathbf{r}) = \langle\hat{\Phi}(\mathbf{r'})\hat{\Phi}(\mathbf{r})\rangle$ is the anomalous density. $\mathcal{L}$ is given by

$$\mathcal{L} = -\frac{\hbar^2}{2m}\nabla^2 - \mu + V_{\text{ext}}(\mathbf{r}) + \int d^3\mathbf{r'}V_{\text{int}}(\mathbf{r}-\mathbf{r'})|\Psi(\mathbf{r'})|^2 + \int d^3\mathbf{r'}V_{\text{int}}(\mathbf{r}-\mathbf{r'})\tilde{n}(\mathbf{r'}) \tag{2.6}$$

A detailed derivation of (2.5) is displayed in the Supplementary information appendix.
We diagonalize (2.6) by employing the Bogoliubov transformation over the fluctuation operators

$$\begin{aligned}\hat{\Phi}(\mathbf{r},t) &= \sum_\nu u_\nu(\mathbf{r})\hat{\alpha}_\nu e^{-\frac{iE_\nu t}{\hbar}} - v_\nu^*(\mathbf{r})\hat{\alpha}_\nu^\dagger e^{\frac{iE_\nu t}{\hbar}}\\ \hat{\Phi}^\dagger(\mathbf{r},t) &= \sum_\nu u_\nu^*(\mathbf{r})\hat{\alpha}_\nu^\dagger e^{\frac{iE_\nu t}{\hbar}} - v_\nu(\mathbf{r})\hat{\alpha}_\nu e^{-\frac{iE_\nu t}{\hbar}}\end{aligned} \tag{2.7}$$

where $\hat{\alpha}_j$ are the quasiparticle operators which satisfy $[\hat{\alpha}_j, \hat{\alpha}_k] = [\hat{\alpha}_j^\dagger, \hat{\alpha}_k^\dagger] = 0$, and u_ν and v_ν denote the Bogoliubov quasiparticle and quasihole amplitudes, respectively. We choose to describe the time dependency by employing a flat phase (independent of the space) introducing E_ν, which corresponds to the energy of the quasi-particle excitation. It is worth remarking that this expansion represents a canonical transformation if it satisfies

$$\int d^3\mathbf{r}\left[u_j^*(\mathbf{r})u_k(\mathbf{r}) - v_j^*(\mathbf{r})v_k(\mathbf{r})\right] = \delta_{jk} \tag{2.8}$$

and

$$\int d^3\mathbf{r}\left[u_j(\mathbf{r})v_k(\mathbf{r}) - u_k(\mathbf{r})v_j(\mathbf{r})\right] = 0 \tag{2.9}$$

as we impose [22].
As a result, the non-condensed and anomalous densities are written in the form

$$\begin{aligned}
\tilde{n}(\mathbf{r}) &= \sum_\nu \left[\left(|u_\nu(\mathbf{r})|^2 + |v_\nu(\mathbf{r})|^2\right)\langle\hat{a}_\nu^\dagger\hat{a}_\nu\rangle + |v_\nu(\mathbf{r})|^2\right] \\
\tilde{m}(\mathbf{r}) &= \sum_\nu \left[2u_\nu(\mathbf{r})v_\nu^*(\mathbf{r})\langle\hat{a}_\nu\hat{a}_\nu^\dagger\rangle + u_\nu(\mathbf{r})v_\nu^*(\mathbf{r})\right] \\
\tilde{n}(\mathbf{r}',\mathbf{r}) &= \sum_\nu \left[\left(u_\nu^*(\mathbf{r}')u_\nu(\mathbf{r}) + v_\nu^*(\mathbf{r})v_\nu(\mathbf{r}')\right)\langle\hat{a}_\nu^\dagger\hat{a}_\nu\rangle + v_\nu^*(\mathbf{r})v_\nu(\mathbf{r}')\right] \\
\tilde{m}(\mathbf{r}',\mathbf{r}) &= -\sum_\nu \left[\left(u_\nu(\mathbf{r}')v_\nu^*(\mathbf{r}) + u_\nu(\mathbf{r})v_\nu^*(\mathbf{r}')\right)\langle\hat{a}_\nu\hat{a}_\nu^\dagger\rangle + u_\nu(\mathbf{r})v_\nu^*(\mathbf{r}')\right]
\end{aligned} \tag{2.10}$$

See the Supplementary information appendix for further details. Introducing Bose statistics, temperature effects are at play since

$$\langle\hat{\alpha}_j^\dagger\hat{\alpha}_k\rangle = \delta_{jk}N_B(E_j) = \frac{1}{\exp\left[\frac{E_j}{k_B\cdot T}\right] - 1} \tag{2.11}$$

where N_B and k_B are the Boltzmann distribution and constant, respectively. Consequently, thermal effects are purely introduced in (2.5) by not neglecting the non-condensed and anomalous densities (Bogoliubov-Popov approximation suggests the opposite in [10]).

Inserting (2.7) in (2.5) it yields two coupled equations for the quasiparticle and quasihole amplitudes [3]

$$\begin{aligned}
&\mathcal{L}_0 u_\nu(\mathbf{r}) + \int d^3\mathbf{r}' V_{\text{int}}(\mathbf{r}-\mathbf{r}')\Psi^*(\mathbf{r}',t)\Psi(\mathbf{r},t)u_\nu(\mathbf{r}') - \int d^3\mathbf{r}' V_{\text{int}}(\mathbf{r}-\mathbf{r}')\Psi(\mathbf{r}',t)\Psi(\mathbf{r},t)v_\nu(\mathbf{r}') = E_\nu u_\nu(\mathbf{r}) \\
&\mathcal{L}_0 v_\nu(\mathbf{r}) + \int d^3\mathbf{r}' V_{\text{int}}(\mathbf{r}-\mathbf{r}')\Psi(\mathbf{r}',t)\Psi^*(\mathbf{r},t)v_\nu(\mathbf{r}') - \int d^3\mathbf{r}' V_{\text{int}}(\mathbf{r}-\mathbf{r}')\Psi^*(\mathbf{r}',t)\Psi^*(\mathbf{r},t)u_\nu(\mathbf{r}') = -E_\nu v_\nu(\mathbf{r})
\end{aligned} \tag{2.12}$$

where $\mathcal{L}_0 = -\frac{\hbar^2}{2m}\nabla^2 - \mu + V_{\text{ext}}(\mathbf{r}) + \int d^3\mathbf{r}' V_{\text{int}}(\mathbf{r}-\mathbf{r}')|\Psi(\mathbf{r}',t)|^2$. They are the so-called Bogoliubov-de Gennes equations, which provide the energy spectrum.

Thermal effects which arise from the non-condensed and anomalous densities are interpreted as a perturbation $\Delta\mu$ to the chemical potential μ . For the later analysis of (2.5), we call

$$\begin{aligned}
\Lambda(\mathbf{r}) &= \int d^3\mathbf{r}' V_{\text{int}}(\mathbf{r}-\mathbf{r}')(|\Psi(\mathbf{r}')|^2 + \tilde{n}(\mathbf{r}')) \\
\Delta\mu(\mathbf{r})\Psi(\mathbf{r}) &= \left(\Omega_n(\mathbf{r}) + \Omega_m(\mathbf{r})\right)\Psi(\mathbf{r}) \\
&= \int d^3\mathbf{r}' V_{\text{int}}(\mathbf{r}-\mathbf{r}')\tilde{n}(\mathbf{r}',\mathbf{r})\Psi(\mathbf{r}') + \int d^3\mathbf{r}' V_{\text{int}}(\mathbf{r}-\mathbf{r}')\tilde{m}(\mathbf{r}',\mathbf{r})\Psi^*(\mathbf{r}')
\end{aligned} \tag{2.13}$$

Therefore, by considering thermal effects, (2.5) is rewritten in the form

$$\left[-\frac{\hbar^2}{2m}\nabla^2 - \mu + V_{\text{ext}}(\mathbf{r}) + \Lambda(\mathbf{r}) + \Delta\mu(\mathbf{r})\right]\Psi(\mathbf{r}) = 0 \tag{2.14}$$

It is noticeable that long range interactions depicted by a dipole-dipole exchange term in V_{int} present a significant challenge: equation (2.14) is an integro-differential equation. Neglecting the thermal fluctuation

and setting the non-condensed density to 0 as [26] suggests the resolution by iterative methods becomes affordable as thermal interactions are typically much more dilute than the condensed density. However, alternatively the non-condensed density is not neglected by introducing the Local Density Approximation (LDA) [22].

2.3 Local Density Approximation

Upon the assumption that the condensate density and external potential are slowly varying, we introduce the LDA presented below

$$u_j(\mathbf{r}) \to u(\mathbf{r},\mathbf{k})e^{i\mathbf{k}\cdot\mathbf{r}} \;\; ; \;\; E_j \to E(\mathbf{r},\mathbf{k}) \;\; ; \;\; \sum_{\mathbf{k}} \to \int \frac{d^3\mathbf{k}}{(2\pi)^3} \tag{2.15}$$

where the prefactor $\frac{1}{(2\pi)^3}$ is included by means of normalization in the Fourier space. Due to the translation invariance, momentum is a good quantum number, then states are labeled with the wavevector $\mathbf{k}$ [22]. Therefore, Bogoliubov amplitudes now include a complex phase dependent of $\mathbf{k}$ as we introduce $u(\mathbf{r},\mathbf{k}) = u_{\mathbf{k}}e^{i\mathbf{k}\cdot\mathbf{r}}$ and $v(\mathbf{r},\mathbf{k}) = v_{\mathbf{k}}e^{i\mathbf{k}\cdot\mathbf{r}}$ where $u_{\mathbf{k}}$ and $v_{\mathbf{k}}$ are constant amplitudes. Furthermore, $V_{\text{int}} \to \tilde{V}_{\text{int}}$, this is, we take the Fourier transform of V_{int} since we move from the real to the complex space. However, it is worth remarking that the LDA fails if the condensed density varies with a length scale larger than the interaction range. Therefore, the thermal terms of (2.13) become

$$\begin{aligned}
\Omega_n(\mathbf{r}) &= \int d^3\mathbf{k}(2\pi)^3\tilde{V}_{\text{int}}(\mathbf{k})\left\{|v(\mathbf{r},\mathbf{k})|^2 + N_B(E(\mathbf{r},\mathbf{k}))\left[|u(\mathbf{r},\mathbf{k})|^2 + |v(\mathbf{r},\mathbf{k})|^2\right]\right\} \\
\Omega_m(\mathbf{r}) &= \int \frac{d^3\mathbf{k}}{(2\pi)^3}\tilde{V}_{\text{int}}(\mathbf{k})\left\{-u(\mathbf{r},\mathbf{k})v^*(\mathbf{r},\mathbf{k}) - 2N_B(E(\mathbf{r},\mathbf{k}))u(\mathbf{r},\mathbf{k})v^*(\mathbf{r},\mathbf{k})\right\}
\end{aligned} \tag{2.16}$$

The Fourier transform of the interaction potential is written out in the form

$$\tilde{V}_{\text{int}}(\mathbf{k}) = g\left[1 + \epsilon_{dd}(3\cos^2(\vartheta(\mathbf{k})) - 1)\right] = g\left[1 + \epsilon_{dd}\left(3\frac{k_y^2}{k_r^2 + k_y^2} - 1\right)\right] \tag{2.17}$$

A full derivation of (2.17) is found in [4]. Here, ϑ accounts for the angle between the polarization direction of the dipole and the $\mathbf{k}$ vector. It is considered dipoles are aligned in the y-direction, such that the k-dependency is captured by the transverse modes k_r and the longitudinal modes k_y. We do not demonstrate (2.17) since it is not the aim of the present work. Therefore, upon LDA (2.12) becomes algebraic [3]

$$\begin{aligned}
\epsilon_{\mathbf{k}}u(\mathbf{r},\mathbf{k}) + n_0(\mathbf{r})\tilde{V}_{\text{int}}(\mathbf{k})u(\mathbf{r},\mathbf{k}) - n_0(\mathbf{r})\tilde{V}_{\text{int}}(\mathbf{k})v(\mathbf{r},\mathbf{k}) &= E(\mathbf{r},\mathbf{k})u(\mathbf{r},\mathbf{k}) \\
\epsilon_{\mathbf{k}}v(\mathbf{r},\mathbf{k}) + n_0(\mathbf{r})\tilde{V}_{\text{int}}(\mathbf{k})v(\mathbf{r},\mathbf{k}) - n_0(\mathbf{r})\tilde{V}_{\text{int}}(\mathbf{k})u(\mathbf{r},\mathbf{k}) &= -E(\mathbf{r},\mathbf{k})v(\mathbf{r},\mathbf{k})
\end{aligned} \tag{2.18}$$

where we have employed $\mathcal{L}_0u(\mathbf{r},\mathbf{k}) = \epsilon_{\mathbf{k}}u(\mathbf{r},\mathbf{k})$ and $\mathcal{L}_0v(\mathbf{r},\mathbf{k}) = \epsilon_{\mathbf{k}}v(\mathbf{r},\mathbf{k})$, where $\epsilon_{\mathbf{k}} = \frac{\hbar^2|\mathbf{k}|^2}{2m}$. Here, $\epsilon_{\mathbf{k}}$ represents the excitation energy of mode $\mathbf{k}$ of the Bogoliubov quasiparticle/quasihole. An analytical solution of the Bogoliubov-de Gennes is accessible depending on the form of the interaction potential. For the case upon consideration, (2.18) directly yields

$$E(\mathbf{r},\mathbf{k}) = \sqrt{\epsilon_{\mathbf{k}}(\epsilon_{\mathbf{k}} + 2n_0(\mathbf{r})\tilde{V}_{\text{int}}(\mathbf{k}))} \tag{2.19}$$

which is the spectrum energy. Under suitable algebraic manipulations [3], the amplitudes take the form

$$\begin{aligned}
|v(\mathbf{r},\mathbf{k})|^2 &= (\epsilon_{\mathbf{k}} + n_0(\mathbf{r})\tilde{V}_{\text{int}}(\mathbf{k}) - E(\mathbf{r},\mathbf{k}))\frac{1}{2E(\mathbf{r},\mathbf{k})} \\
u(\mathbf{r},\mathbf{k})v^*(\mathbf{r},\mathbf{k}) &= n_0(\mathbf{r})\tilde{V}_{\text{int}}(\mathbf{k})\frac{1}{2E(\mathbf{r},\mathbf{k})}
\end{aligned} \tag{2.20}$$

Consequently, from (2.19) we can study low-momenta features of the system. For instance, we obtain the speed of sound by taking the limit $\mathbf{k} \to 0$ of the spectrum [24]. Note that in the high-energy or large momentum regime ($\mathbf{k}\xi >> 1$), the spectrum takes the form of the dispersion relation $\epsilon_{\mathbf{k}}$, this is, as free particles.
Furthermore, depending on the shape of the energy spectrum the system can feature supersolidity by which localized density patterns are formed [33].

So far we have established a mathematical framework to describe the generalized correction terms Ω_m and Ω_n. The aim of the section below is to provide analytical expressions of these components and discuss their role on BEC.

2.4 Thermal and quantum fluctuations

First, we discuss the easiest case which corresponds to the zero-temperature system. In this regime, the Boltzmann distribution $N_B(E)$ tends to zero, therefore every term multiplied by $N_B(E)$ of (2.16) vanishes [3]

$$\begin{aligned}\Omega_n(\mathbf{r})\Psi(\mathbf{r}) &\approx \Psi(\mathbf{r}) \int \frac{d^3\mathbf{k}}{(2\pi)^3} \tilde{V}_{\text{int}}(\mathbf{k}) |v(\mathbf{r},\mathbf{k})|^2 = \frac{8}{3} g n_0(\mathbf{r}) \sqrt{\frac{a_s^3 n_0(\mathbf{r})}{\pi}} \mathcal{Q}_5 \Psi(\mathbf{r}) \\ \Omega_m(\mathbf{r})\Psi(\mathbf{r}) &\approx -\Psi(\mathbf{r}) \int \frac{d^3\mathbf{k}}{(2\pi)^3} \tilde{V}_{\text{int}}(\mathbf{k}) u(\mathbf{r},\mathbf{k}) v^*(\mathbf{r},\mathbf{k}) = 8 g n_0(\mathbf{r}) \sqrt{\frac{a_s^3 n_0(\mathbf{r})}{\pi}} \mathcal{Q}_5 \Psi(\mathbf{r})\end{aligned} \tag{2.21}$$

where $\mathcal{Q}_5$ takes the form $\mathcal{Q}_5(\epsilon_{dd}) = \int_0^1 du[1 + \epsilon_{dd}(3u^2 - 1)]^{\frac{5}{2}}$ after introducing the variable change $u = \cos(\vartheta)$ and noticing it is symmetrical on u (see the Supplementary information appendix). As a result, the generalised Gross-Pitaevskii equation from (2.14) reads [22]

$$\left[-\frac{\hbar^2}{2m}\nabla^2 + V_{\text{ext}}(\mathbf{r}) - \mu + \int d^3\mathbf{r'} V_{\text{int}}(\mathbf{r} - \mathbf{r'})(|\Psi(\mathbf{r'})|^2 + \tilde{n}(\mathbf{r'})) + \frac{32}{3} g \sqrt{\frac{a_s^3}{\pi}} \mathcal{Q}_5(\epsilon_{dd}) |\Psi(\mathbf{r})|^3 \right] \Psi(\mathbf{r}) = 0 \tag{2.22}$$

The last term corresponds to the Lee-Huang-Yang first order correction. These quantum fluctuations were firstly introduced by Lee-Huang-Yang [20] which depend only on the two-body scattering length a_s. Moreover, it shifts the ground state of the condensate as it increases the chemical potential. Furthermore, it has been revealed that it arrests the dipolar collapse [15] providing an extra repulsive term (it is proportional to $n_0(\mathbf{r})^{\frac{3}{2}}$). As a result, a balance between attractive and repulsive interaction may be reached, forming stable quantum droplets by which the density takes a localized profile (they feature liquid-like properties).
Note that further repulsive components such as three-body repulsive interactions can avoid the collapse of the condensate and produce a self-bound droplet as well [14].

As introduced before, Ω_n and Ω_m may be generalized to the finite temperature case. In this way, let's focus firstly on the thermal corrections (components multiplied by $N_B(E)$ as it is dependent on the temperature) in (2.16)

$$\Delta\mu_{\text{TH}} = \int d^3\mathbf{k} N_B(E(\mathbf{r},\mathbf{k})) \left[|u(\mathbf{r},\mathbf{k})|^2 + |v(\mathbf{r},\mathbf{k})|^2 \right] - 2N_B(E(\mathbf{r},\mathbf{k})) u(\mathbf{r},\mathbf{k}) v^*(\mathbf{r},\mathbf{k}) \tag{2.23}$$

where $\Delta\mu_{\text{TH}}$ captures the thermal correction of the chemical potential. Note that as we increase the temperature, more particles leave the condensate, which affects on the stability of droplets. Hence, $\Delta\mu_{\text{TH}}$ is fundamental in the correct description of the finite temperature case even though the total

depleted density is small compared to the condensate.
Therefore, we insert (2.20) in (2.16) to obtain the finite temperature corrections [3]

$$\begin{aligned}\Omega_n(\mathbf{r}) &= \int \frac{d^3\mathbf{k}}{(2\pi)^3}\tilde{V}_{\rm int}(\mathbf{k})\left\{\frac{\epsilon_{\mathbf{k}}+n_0(\mathbf{r})\tilde{V}_{\rm int}(\mathbf{k})-E(\mathbf{r},\mathbf{k})}{2E(\mathbf{r},\mathbf{k}))}+N_B(E(\mathbf{r},\mathbf{k}))\frac{\epsilon_{\mathbf{k}}+n_0(\mathbf{r})\tilde{V}_{\rm int}(\mathbf{k})}{2E(\mathbf{r},\mathbf{k})}\right\}\\ \Omega_m(\mathbf{r}) &= \int \frac{d^3\mathbf{k}}{(2\pi)^3}\tilde{V}_{\rm int}(\mathbf{k})\left\{-\frac{n_0(\mathbf{r})\tilde{V}_{\rm int}(\mathbf{k})}{2E(\mathbf{r},\mathbf{k})}+\frac{n_0(\mathbf{r})\tilde{V}_{\rm int}(\mathbf{k})}{2\epsilon_{\mathbf{k}}}-N_B(E(\mathbf{r},\mathbf{k}))\frac{n_0(\mathbf{r})\tilde{V}_{\rm int}(\mathbf{k})}{E(\mathbf{r},\mathbf{k})}\right\}\end{aligned} \tag{2.24}$$

where we have employed the orthogonality condition on the amplitudes which reads $|u(\mathbf{r},\mathbf{k})|^2-|v(\mathbf{r},\mathbf{k})|^2=1$. Thus, the sum of the fluctuation components becomes

$$\Delta\mu(\mathbf{r})=\Omega_n(\mathbf{r})+\Omega_m(\mathbf{r})=\int\frac{d^3\mathbf{k}}{(2\pi)^3}\tilde{V}_{\rm int}(\mathbf{k})\left\{\frac{\epsilon_{\mathbf{k}}}{2E(\mathbf{r},\mathbf{k})}+\frac{n_0(\mathbf{r})\tilde{V}_{\rm int}(\mathbf{k})}{2\epsilon_{\mathbf{k}}}-\frac{1}{2}+N_B(E(\mathbf{r},\mathbf{k}))\frac{\epsilon_{\mathbf{k}}}{E(\mathbf{r},\mathbf{k})}\right\} \tag{2.25}$$

We aim to express the previous equation in a reescaled form by using a characteristic length of the system. Thus, we define the *healing length* as $\xi=\frac{\hbar}{\sqrt{2mgn_0}}$, which is obtained by equalling the following terms ([1])

$$\frac{\hbar^2}{2m}\nabla^2\Psi(\mathbf{r})=gn_0\Psi(\mathbf{r})\rightarrow\frac{\hbar^2}{2m}\frac{1}{\xi^2}=gn_0\rightarrow\xi=\frac{\hbar}{\sqrt{2mgn_0}} \tag{2.26}$$

Note that since $n_0(\mathbf{r})=|\Psi(\mathbf{r})|^2$, the *healing length* is proportional to $\frac{1}{|\Psi(\mathbf{r})|}$. Moreover, as [3] suggests, it is introduced by means of a spherical cutoff of radius k_c in the $\mathbf{k}$-space in the $\mathbf{k}$-integrals discussed (see Fig. 2.1).

As we expect, the previous cutoff removes the condensate instability for low momenta values where the integrand becomes imaginary, such that the system will only support excitations of wave vectors which exceed the cutoff (finiteness of the system is considered). Note that these instabilities arise from the limitations of our approximations and do not correspond to real physical situation. As a result, by an adequate cutoff long wavelengths are no longer supported. Alternatively, a simple rectangular cutoff [28] provides similar results by taking $k_r\in[0.012,0.05]/\xi$ and $k_y\in[0.007,0.009]/\xi$, where we set ξ to $\xi=1.43a_s$. In Fig. 2.2 we can visualize the cutoff region in comparison with the regimes where the divergence is produced.
Other cutoffs have appeared in the current literature [5][27] which provide quantitatively similar results. Moreover, we introduce $k=\frac{q}{\xi}$, $\cos(\vartheta)=u$, $f(u)=1+\epsilon_{dd}(3u^2-1)$ and $t(\mathbf{r})=\frac{k_BT}{gn_0(\mathbf{r})}$ as the normalized temperature. Thus, the fluctuation term is rewritten in the form [3]

$$\begin{aligned}\Delta\mu(\mathbf{r}) &= \frac{g}{4\pi^2\xi^3}\int_{-1}^{1}du\int_{q_c}^{\infty}q^2dqf(u)\\ &\times\left\{\frac{q^2}{2\sqrt{q^2(q^2+2f(u))}}+\frac{f(u)}{2q^2}-\frac{1}{2}+\frac{1}{\exp[\sqrt{q^2(q^2+2f(u))}/t(\mathbf{r})]-1}\times\frac{q^2}{\sqrt{q^2(q^2+2f(u))}}\right\}\end{aligned} \tag{2.27}$$

We provide further details on the derivation in the Supplementary information appendix. After manipulating and inserting $\xi=\frac{\hbar}{\sqrt{2mgn_0}}=\frac{\hbar}{\sqrt{2mg}}\frac{1}{|\Psi|}$ in the previous equation, the chemical fluctuation becomes (see also the Supplementary information appendix)

$$\Delta\mu(\mathbf{r})=\frac{32}{3}g\sqrt{\frac{a_s^3}{\pi}}[\mathcal{Q}_5(\epsilon_{dd})+\mathcal{R}(\epsilon_{dd},t(\mathbf{r}))]|\Psi(\mathbf{r})|^3=H_{\rm qu}(\mathcal{Q}_5)+H_{\rm th}(\mathcal{R}) \tag{2.28}$$

[1]Note that since n_0 depends on $\mathbf{r}$, ξ shall be a function of $\mathbf{r}$ as well. However, it is used in the current literature as a length unit, therefore we will write ξ instead of $\xi(\mathbf{r})$.

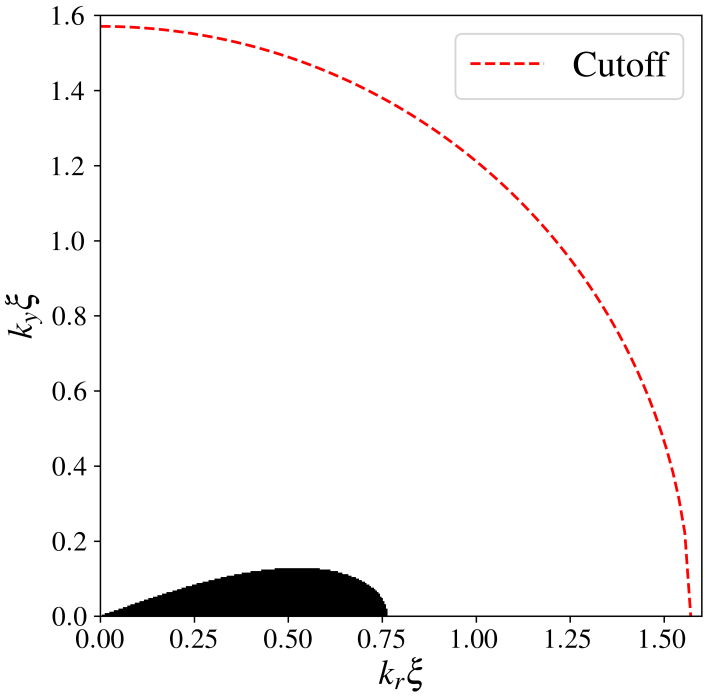

Figure 2.1: Spherical **k** cutoff. Black area represents the collapsing modes, where the dispersion relation becomes imaginary. For the calculations we set $a_s = 82.7a_0$, $\epsilon_{dd} = 1.5$ and $n_0 = 6 \times 10^6 \mu m^{-3}$.

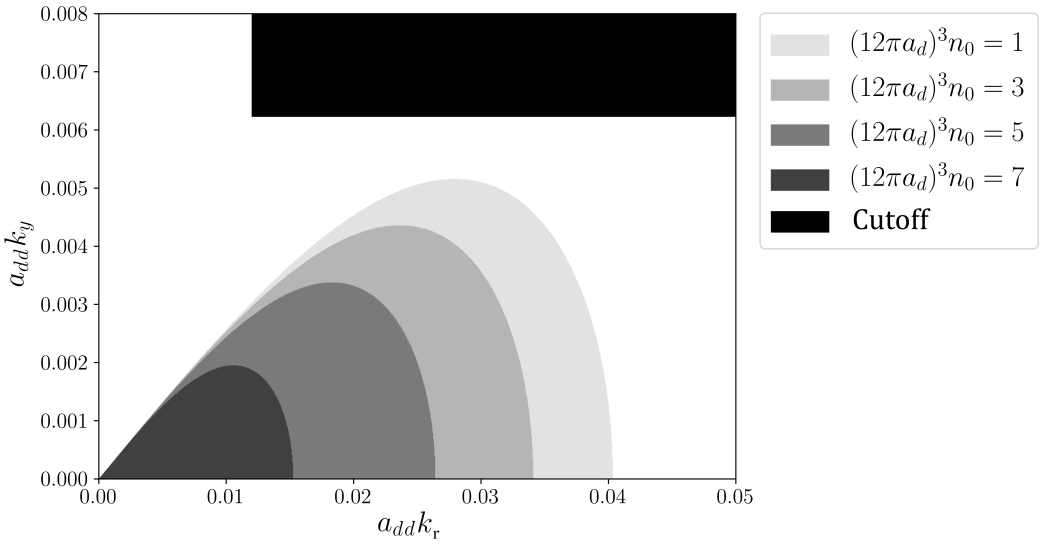

Figure 2.2: Rectangular **k** cutoff. The overlayed grey shaded areas indicate the momentum-space regions where $\epsilon_{\mathbf{k}}$ becomes imaginary for a range of values of n_0. The black shaded area is the cutoff employed in the present work.

where

$$\begin{aligned}\mathcal{Q}_5(\epsilon_{dd};q_c) &= \frac{1}{4\sqrt{2}}\int_0^1 du f(u)\left[(4f(u)-q_c^2)\sqrt{2f(u)+q_c^2}-3f(u)q_c+q_c^3\right]\\ \mathcal{R}(\epsilon_{dd},t;q_c) &= \frac{3}{4\sqrt{2}}\int_0^1 du\int_{q_c^2}^{\infty} dQ\frac{Qf(u)}{\sqrt{Q+2f(u)}}\frac{1}{\exp[\sqrt{Q(Q+2f(u))}/t]-1}\end{aligned} \tag{2.29}$$

Here, $q_c = k_c\xi$ and $k_c = \frac{\pi}{2\xi}$, which captures the inverse coherent length of the condensate [3]. One can easily find that it yields $q_c = \frac{\pi}{2}$.

So far, we have obtained the fluctuation correction after inserting Bogoliubov amplitudes upon LDA in (2.24). We proceed to insert now the amplitudes obtained in (2.20) into the depleted density $\tilde{n}(\mathbf{r})$ of (2.10) within the same LDA. It yields

$$\tilde{n}(\mathbf{r}) = \int \frac{d^3\mathbf{k}}{(2\pi)^3}(|v(\mathbf{r},\mathbf{k})|^2 + N_B(E(\mathbf{r},\mathbf{k}))[|u(\mathbf{r},\mathbf{k})|^2+|v(\mathbf{r},\mathbf{k})|^2]) \tag{2.30}$$

Using the Bogoliubov amplitudes relations found in (2.20), the depleted density is written out in the form

$$\tilde{n}(\mathbf{r}) = \frac{8}{3}g\sqrt{\frac{a_s^3}{\pi}}(\mathcal{Q}_3(\epsilon_{dd})+\mathcal{P}(\epsilon_{dd},t(\mathbf{r})))|\Psi(\mathbf{r})|^3 \tag{2.31}$$

where

$$\begin{aligned}\mathcal{Q}_3(\epsilon_{dd};q_c) &= \frac{1}{\sqrt{2}}\int_0^1 du f(u)[(f(u)-q_c^2)\sqrt{2f(u)+q_c^2}+q_c^3]\\ \mathcal{P}(\epsilon_{dd},t;q_c) &= \frac{3}{\sqrt{2}}\int_0^1 du\int_{q_c^2}^{\infty} dQ\frac{Q+f(u)}{\sqrt{Q+2f(u)}}\frac{1}{\exp[Q\sqrt{Q(Q+2f(u))}/t]-1}\end{aligned} \tag{2.32}$$

By setting $t = 0$, the fluctuation component becomes purely quantum and it matches what was obtained in (2.22), reobtaining the zero temperature result (see the Supplementary information appendix).
We plot $\tilde{n}$ as function of the reduced temperature t in Fig. 2.3. One finds that as we increase the temperature more particles leave the condensate. Moreover, at very low temperatures $\tilde{n}$ is constant until thermal fluctuations become relevant. This component remains small and according to Popov approximation it can be neglected since the condensed density is much larger (even though $\tilde{n}$ is proportional to $n_0^{\frac{3}{2}}$, the conservation of the total density n ($n = n_0 + \tilde{n}$) is still satisfied). We gain further insights by visualizing the chemical potential fluctuation along the quantum ($\mathcal{Q}_3$) and thermal ($\mathcal{R}$) fluctuation components depicted in Fig. 2.4.

As we observe in Fig. 2.4, the quantum perturbation remains constant while the thermal correction reaches a minimum at $t = 1$ and raises as the temperature increases (see panel (b)). This minimum yields a chemical potential correction smaller than if only quantum fluctuations were considered. In fact, at $t = 1$ thermal energy matches the energy from repulsive interaction between particles ($t = 1 \rightarrow k_BT = gn_0$). We can investigate the temperature where this occurs: by setting $a_s = 87.2a_0$ and $n_0 = 6\ \mu m^{-3}$ the previous phenomenon is observed at $T = 103.036$ nK.
Given the role of fluctuations as functions dependent of the temperature, we also find that the quantum correction is proportional to $n^{\frac{3}{2}}$ ($|\Psi(\mathbf{r})|^3$), while the thermal scales like $n^{\frac{3}{2}}$ times a component $\mathcal{R}$ which decreases as n raises.

This phenomenon supports the formation of roton quasiparticles as [28] suggests. They were introduced by Landau [13] as elementary vortices to describe superfluidity in ^{4}He. They induce pattern formation by which particles tend to gather in spots. Surprisingly, raising the temperature leads to a phase-transition in which particles are distributed in a periodic lattice, which is counter intuitive since

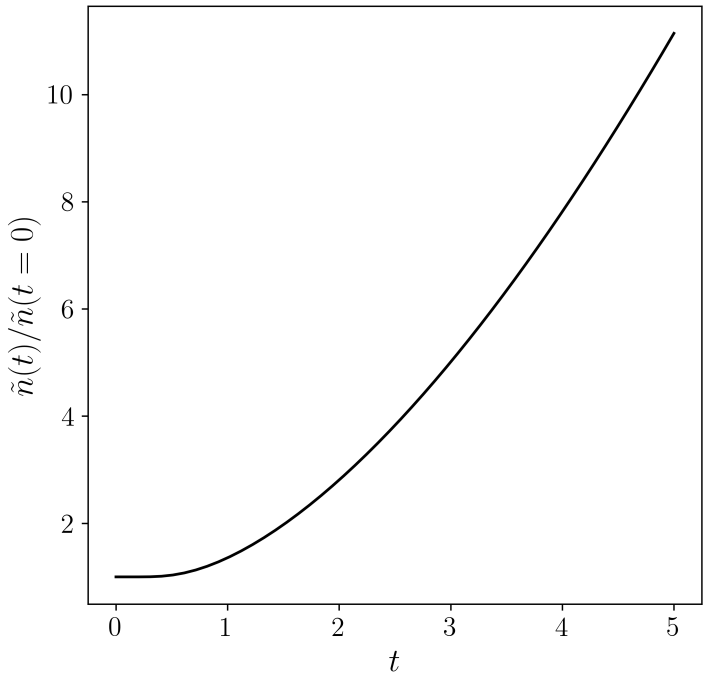

Figure 2.3: Depleted density as a function of the reduced temperature t. For the plot we have set m to the mass of Dy, $a_s = 87.2a_0$, and $\epsilon_{dd} = 1.5$.

raising the temperature enhances the thermal motion of particles [28].

As discussed before, the depleted density is typically much smaller than the condensed density, therefore we insert (2.28) in (2.22) and neglect the component multiplied by $\tilde{n}$, such that the local chemical fluctuation, which encompasses quantum and thermal corrections, becomes

$$\left[h_0 + \int d^3\mathbf{r} V_{\text{int}}(\mathbf{r}-\mathbf{r}')|\Psi(\mathbf{r}')|^2 + \Delta\mu(\mathbf{r})\right]\Psi(\mathbf{r}) = 0 \tag{2.33}$$

where $\Delta\mu$ corresponds to (2.28) and $h_0 = -\frac{\hbar^2}{2m}\nabla^2 + V_{\text{ext}}(\mathbf{r}) - \mu$, which captures the free energy particle contribution (kinetic energy plus a confining potential).
From Fig. 2.4 we observe $\mathcal{R}$ scales proportional to t^2, therefore we approach the thermal fluctuation component as a function $\mathcal{S}(\epsilon_{dd}) \times t^2$. This choice is supported in [3], where it is observed that a t^n curve with $n > 2.5$ produces a divergence when the reduced temperature is high. Moreover, the t^2 approximation well describes the thermal fluctuation for the range $0 < t < 10$, which results in a finite correction. In order to obtain $\mathcal{S}(\epsilon_{dd})$, we plot $\mathcal{S}$ as a function of ϵ_{dd} and fit it to a polynomial of 2^{th} order. The optimal fit is $\mathcal{S}(\epsilon_{dd}) = -0.158985\epsilon_{dd}^2 + 0.324529\epsilon_{dd} - 0.0158037$. In this way, (2.34) is rewritten in a compact form

$$\left[-\frac{\hbar^2}{2m}\nabla^2 + V_{\text{ext}}(\mathbf{r}) + \int d^3\mathbf{r}' V_{\text{int}}(\mathbf{r}-\mathbf{r}')|\Psi(\mathbf{r}')|^2 + \gamma|\Psi(\mathbf{r})|^3 + \Theta T^2 \frac{1}{|\Psi(\mathbf{r})|} - \mu\right]\Psi(\mathbf{r}) = 0 \tag{2.34}$$

where $\gamma = \frac{32}{3} g\sqrt{\frac{a_s^3}{\pi}}\mathcal{Q}_5(\epsilon_{dd})$ and $\Theta = \frac{32}{3} g\sqrt{\frac{a_s^3}{\pi}}\frac{k_B^2}{g^2}\mathcal{S}(\epsilon_{dd})$. Note that in the thermal component we have employed $t = \frac{k_B T}{g n_0}$ and $n_0(\mathbf{r}) = |\Psi(\mathbf{r})|^2$. Finally, in order to obtain the energy functional $E[\Psi]$ from

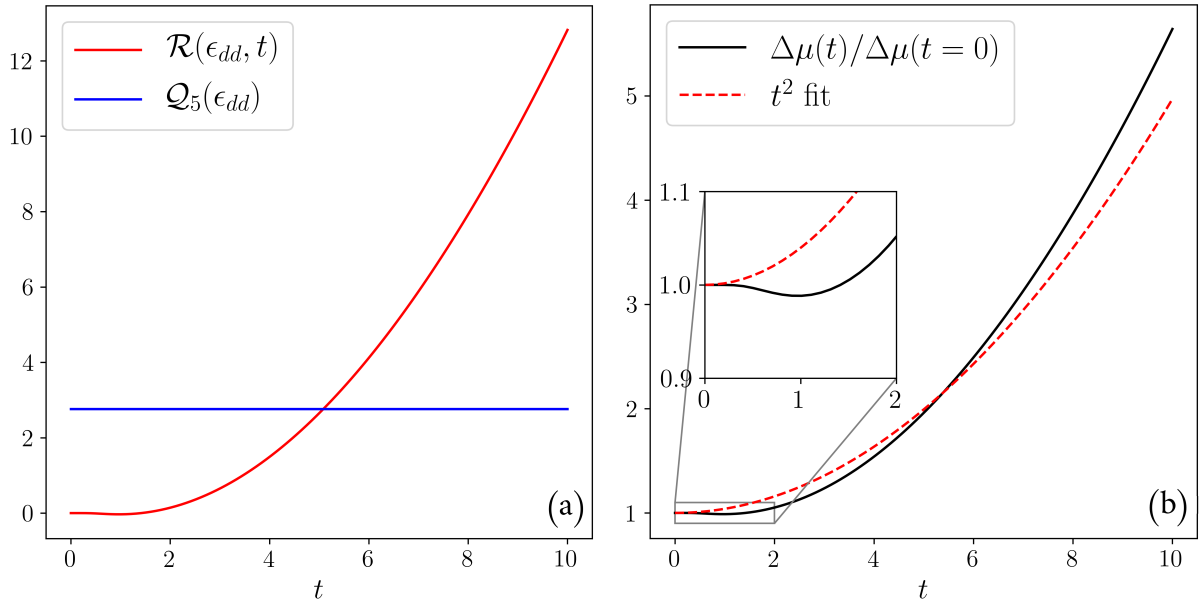

Figure 2.4: (a) Thermal and quantum corrections by the $\mathcal{R}(\epsilon_{dd}, t)$ and $\mathcal{Q}_5(\epsilon_{dd})$ unitless functions. (b) Local chemical potential fluctuation. Inset of panel (b) shows the behaviour of the chemical potential fluctuation at $t = 1$ in comparison with the t^2 fit. For the calculations we fixed values $\epsilon_{dd} = 1.5$ and $a_{dd} = 130.8a_0$.

which we can extract the phase diagram, we use that $E[\Psi]$ is minimal in equilibrium, therefore it satisfies $\frac{\delta E[\Psi]}{\delta \Psi^*} = 0$ where $\frac{\delta}{\delta \Psi^*}$ is the functional derivative. Hence, we must find $E[\Psi]$ such that yields (2.34). One finds that $E[\Psi]$ is expressed in the form (see the Supplementary information appendix) [3]

$$E[\Psi] = \int d^3\mathbf{r}\Psi^*(\mathbf{r}) \left[-\frac{\hbar^2}{2m}\nabla^2 + V_{\text{ext}}(\mathbf{r})\right] \Psi(\mathbf{r}) + \frac{1}{2}\int d^3\mathbf{r} \int d^3\mathbf{r'}|\Psi(\mathbf{r})|^2 V_{\text{ext}}(\mathbf{r}-\mathbf{r'})|\Psi(\mathbf{r'})|^2 + \frac{2}{5}\int d^3\mathbf{r}\gamma|\Psi(\mathbf{r})|^5 + 2\int d^3\mathbf{r}\Theta T^2|\Psi(\mathbf{r})| \tag{2.35}$$

where first term comprises the free particle motion under a trapping potential V_{ext}, the second yields the interaction between particles which encompasses s-wave scattering as well as long ranged dipolar interactions, the third features quantum fluctuations (independent of the temperature) and the last captures the thermal fluctuations due to finite temperatures. The previous equation opens the door for exploring the thermodynamics of the dipolar BEC: it provides the energy of the condensed particle given a wavefunction $\Psi(\mathbf{r})$. Employing a simple variational approximation, we are now able to study the phase diagram from which we can visualize the superfluidity phenomenon as we modify the interaction length and the particle density. We will also provide insights on the realization of insulated droplets.

In the next chapter we aim to provide further details on the geometry of the system upon consideration, as well as stochastic methods by which we can approach the minimization of (2.35) choosing an adequate wavefunction $\Psi(\mathbf{r})$ which captures the physics of the condensate.

Chapter 3

Methods

We consider a dipolar Bose-gas confined in a cylinder geometry along the z-axis such that dipoles are aligned in the y-direction by an external field [6] (see Fig. 3.1).

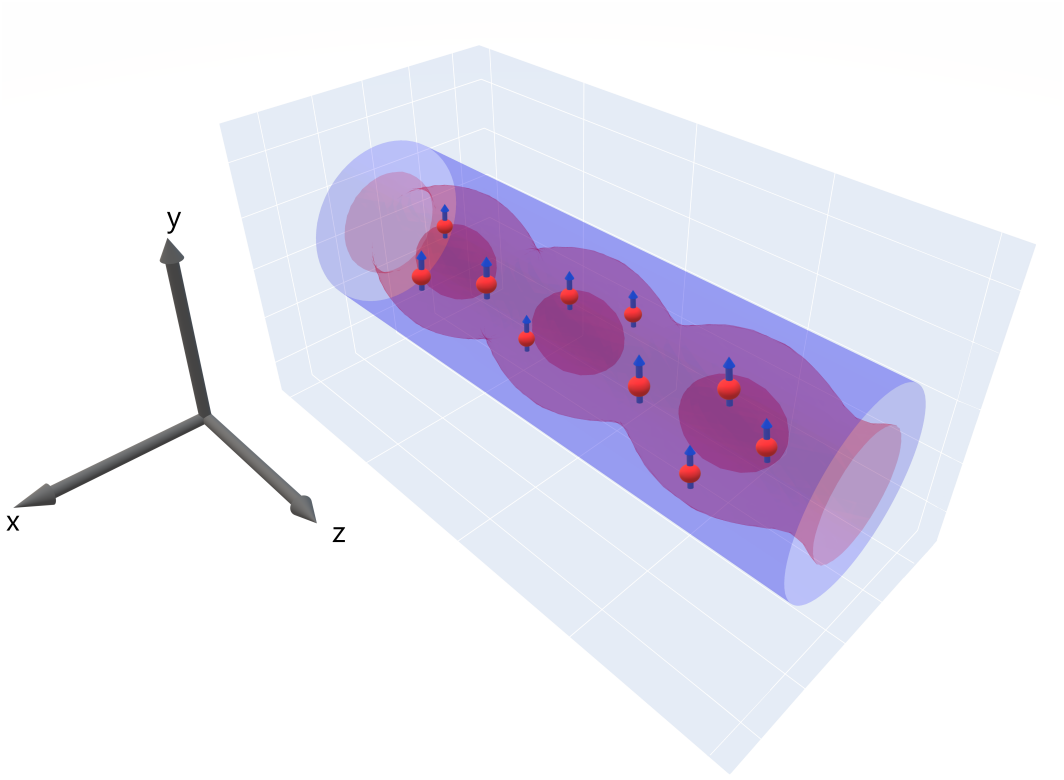

Figure 3.1: Schematic sketch of the geometry upon consideration. The dipoles are aligned in the y-direction, the density confined in the x and y-direction. The depcited surfaces illustrate isodensity surfaces of the density $|\Psi|^2$.

They are trapped in a transverse harmonic potential with freedom of movement along the z-direction.

Hence, the external potential V_{ext}, as a function of the spatial transverse variables, becomes

$$V_{\text{ext}} = \frac{1}{2}m\left(\omega_x x^2 + \omega_y y^2\right) \tag{3.1}$$

where ω_x and ω_y are the angular frequencies of the confinement. We set $\omega_{x,y} = 2\pi \times 150$ Hz, as used in the experiments [6, 31] ([1]). Following [6], we split the wavefunction Ψ as $\Psi(\mathbf{r}) = \chi(x,y)\psi(z)$, where the condensate wavefunction is decomposed into an axial field ($\psi(z)$) and a transverse part ($\chi(x,y)$). For the latter, we employ the Gaussian approximation by which $\chi(x,y)$ is described variationally as $\chi(x,y) = \frac{1}{\sqrt{\pi}l}\exp\left[-(\eta x^2 + y^2/\eta)/2l^2\right]$, where l and η capture its mean and anisotropy, respectively. For the longitudinal part, we shall discuss an ansatz which properly describes the axial wavefunction. As [6] underlines, at low densities the system can undergo a discontinuous and continuous transition between the insulating droplet and the unmodulated density state. At higher densities continuity on the superfluid-supersolid transition may be accessible [33]. In the present work, we focus on the latter for which a cosine-like ansatz is reasonable ([2]). Therefore, the axial wavefunction is described as [6]

$$\psi(z) = \sqrt{n_z}\left(\cos\theta + \sqrt{2}\sin\theta\cos\frac{2\pi z}{L}\right) \tag{3.2}$$

where n_z is the axial density. In (3.2), θ and L are treated as variational parameters, where the first denotes the amplitude of the density modulation and the latter captures the wavelength of the modulation. With the variational parameter L, $\psi(z)$ is defined on a unit cell of length $-\frac{L}{2} \leq z < \frac{L}{2}$ subject to the normalization constraint $\int_{uc} dz|\psi(z)|^2 = n_z L$, where uc stands for unit cell. Note the system is not confined in the z-direction. Moreover, θ is restricted to the range $\theta \in [0, \cot^{-1}(\sqrt{2})]$. We also define the density contrast $\mathcal{C}$ as $\mathcal{C} = \frac{|\Psi|^2_{max} - |\Psi|^2_{min}}{|\Psi|^2_{max} + |\Psi|^2_{min}}$ where $|\Psi|_{max}$ and $|\Psi|_{min}$ are the maximum and minimum of $|\Psi|$. Note that $\mathcal{C}$ is strictly an increasing function of θ in the range employed. Moreover, θ is constrained such that $\mathcal{C}$ is defined in the range $[0,1]$. By substituting the axial and transverse wavefunctions discussed previously, we find θ describes the density contrast as $\mathcal{C} = \frac{2\sqrt{2}\sin(2\theta)}{3-\cos(2\theta)}$. Hence, when $\mathcal{C} = 0$ the system is in the unmodulated phase, where the ground state is uniform, while for $\mathcal{C} = 1$ the system features a completely modulated axial density. By inserting the previously described wavefunction in (2.35) and numerically minimizing the energy functional for the variational parameters $\{l, \eta, \theta, L\}$ we obtain the phase diagram from which we can discern the transition between the density modulated and unmodulated states, analyzing the striking role of temperature. We will analyze the transition regime for $n_z \in [0.165, 8.6] \times 10^3 \mu m^{-1}$ and $a_s \in [80, 94] \times a_0$.
For the minimization we employ the *Basin-hopping* algorithm provided by the *Python* library *sicpy.optimize*.

Furthermore, the boundaries of the variational parameters are initially set to

$$\eta \in [2.6, 7.4]\ ;\ l \in [0.7, 1.5]\ \mu m\ ;\ L \in [0.6, 3.0]\ \mu m\ ;\ \theta \in [0, \cot^{-1}(\sqrt{2})] \tag{3.3}$$

such that the initial guess is chosen to be the center value of the previous ranges. This choice provides qualitatively good results which are in agreement with [6] for $T = 0$. However, as we raise the temperature, we observed the numerical method gets stuck in local minima. For that matter, we used the minimized parameters obtained in the previous iteration as the initial guess of the next. Furthermore, we constrain the boundaries of the next iteration to a certain range centered in the minimized parameters yielded by the previous (these boundaries are not constant, and we have modified them for different regions of the phase diagram which proved to provide better results). After a row loop, boundaries are set back to (3.3). This calculation is extended to all rows and columns of a 100×100 points grid.

[1] The choice of the confinement frequencies is not trivial: having tighter confinement along a specific direction can induce an additional discontinuous transition as [6] suggests.

[2] This ansatz is not always reasonable, in particular when the transition is of first order.

In the next chapter we provide numerically the phase diagrams obtained from the t^2 approximation for a range of different temperatures and discuss the physical phenomena at play. Furthermore, we compare the quantum and thermal fluctuations from (2.28).

Chapter 4

Results and discussions

We obtain the phase diagram by variationally minimizing the energy functional for a range of temperatures $T = \{0, 25, 50, 75, 100\}$ nK to illustrate the underlying physical effect of introducing finite temperatures. We also obtain numerically the quantum and thermal corrections as functions of the density.

4.1 Zero-temperature phase diagram

First, we discuss the zero-temperature case which is depicted in Fig. 4.1. In this regime, only quantum fluctuations due to the depleted density are taken in account [30].

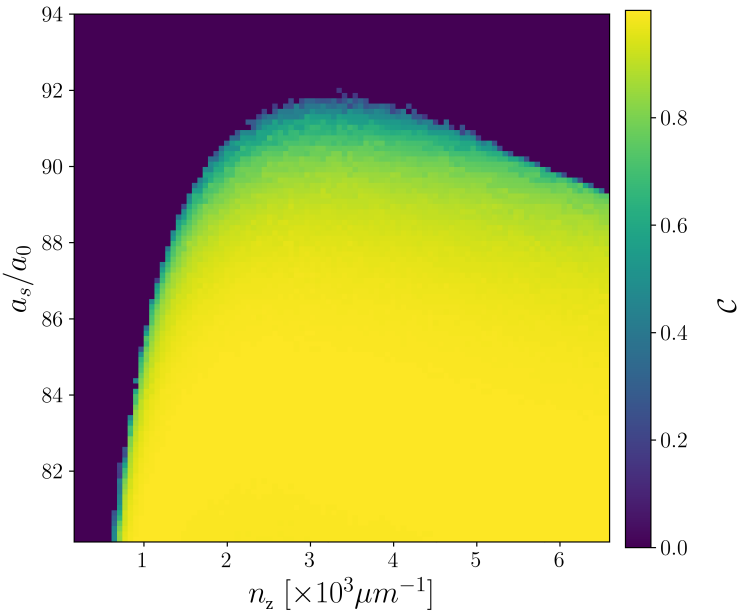

Figure 4.1: Phase diagram for the zero-temperature case displaying the contrast $\mathcal{C}$ as a function of n_z and a_s. Parameters are fixed to $m = m_{Dy}$ and $a_{dd} = 130.8a_0$.

We can visualize the phase diagram splits into three regions depending on $\mathcal{C}$: unmodulated density ($\mathcal{C} \approx 0$), modulated density ($0 < \mathcal{C} \ll 1$) and insulated droplets ($\mathcal{C} \approx 1$).

In the first region, it is satisfied $\mathcal{C} = 0$ ($\theta = 0$), therefore the axial wavefunction along the z-axis becomes $\psi(z) = \sqrt{n_z}$. Consequently, the axial wavefunction profile is purely independent of the z variable, and the axial density $|\Psi|^2$ is constant along the z-axis. This yields a unmodulated density profile. Furthermore, we observe that as we decrease the axial density (for $n_z < 2 \times 10^3 \mu m^{-1}$) the system enters the unmodulated states for a larger number of scattering lengths.

In the third region, we observe $\mathcal{C} \approx 1$ ($\theta \approx \cot^{-1}(\sqrt{2})$), therefore from the definition of $\mathcal{C}$ one finds $|\Psi|^2_{min} = 0$. Consequently, bosons tend to gather in localized insulated droplets and particles can not move along the z-axis, this is, superfluidity is not accessible. The formation of isolated droplets is produced by the quantum fluctuations introduced by LHY components. Note that this region is not accessible if quantum fluctuations are not considered [33], where the system collapses .

Finally, in the second region $\mathcal{C}$ satisfies $0 < \mathcal{C} \ll 1$. As an intermediate state between the unmodulated superfluid and isolated droplets, it features supersolidity in which fluid (unmodulated density) and solid (supersolid) properties are present simultaneously, where the discrete translational symmetry occurs. In this regime, the axial density develops a weakly modulated cosine like behavior as we increase $\mathcal{C}$ and enters the modulated density regime. We also observe that only a limited number of values n_z and a_s produce supersolidity: this arises from the balance between long-range and short-range interactions.

Moreover, we identify a discontinuous transition between the unmodulated superfluid and isolated droplets for small and large density values (1^{st} order transition, from a qualitative look at the sharp gradient of colors in the splitting border of the phase diagram). In these regimes, the density modulation is sensible to variations of n_z (for low densities) and a_s (for large densities). However, supersolidity is featured at a certain range of values n_z and a_s in which the unmodulated phase evolves to weakly modulated states smoothly (2^{nd} order transition, from a qualitative look at the smooth gradient of colors in the splitting border of the phase diagram). Analytically, we can derive the condition by which a continuous transition is produced from analyzing the stationary points of the minimized energy functional for small θ [6]. Hence, we obtained that the regime of supersolidity can be expected to be close to the region where the phase transition is of 2^{nd} order. This region can be well described by a roton excitation ansatz for a critical scattering length a_{rot}. This is sometimes referred to as Turing instability in other contexts. Consequently, the roton-softening is observed to occur at $a_{rot} = 91.6a_0$, which matches the regime in which supersolidity evolves to unmodulated superfluid, consistent with [6]. As [30] suggests, the roton formation marks the instability of the unmodulated density region and thus characterises the phase diagram, such that a pattern in the density distribution can be realized.

In the next section we aim to analyze the finite temperature phase diagrams (for $T = \{25, 50, 75, 100\}$ nK) by inserting thermal fluctuations in the energy functional. We also provide numerics on the calculations of the thermal and quantum fluctuations at finite temperatures.

4.2 Finite temperature phase diagram

The phase diagrams obtained for $T \in \{25, 50, 75, 100\}$ nK are displayed in Fig. 4.2.

Upon increasing the temperature, a discernible shift of the separating border between modulated states and superfluid towards higher scattering lengths and lower densities is observed (see Fig. 4.3). Therefore, a higher degree of modulation is produced as temperature raises, facilitating the formation of a supersolid state accessible for finite temperatures (see Fig. 4.4). This behavior is surprising since raising the temperature is expected to melt the supersolid state. In this work, we observe the opposite:

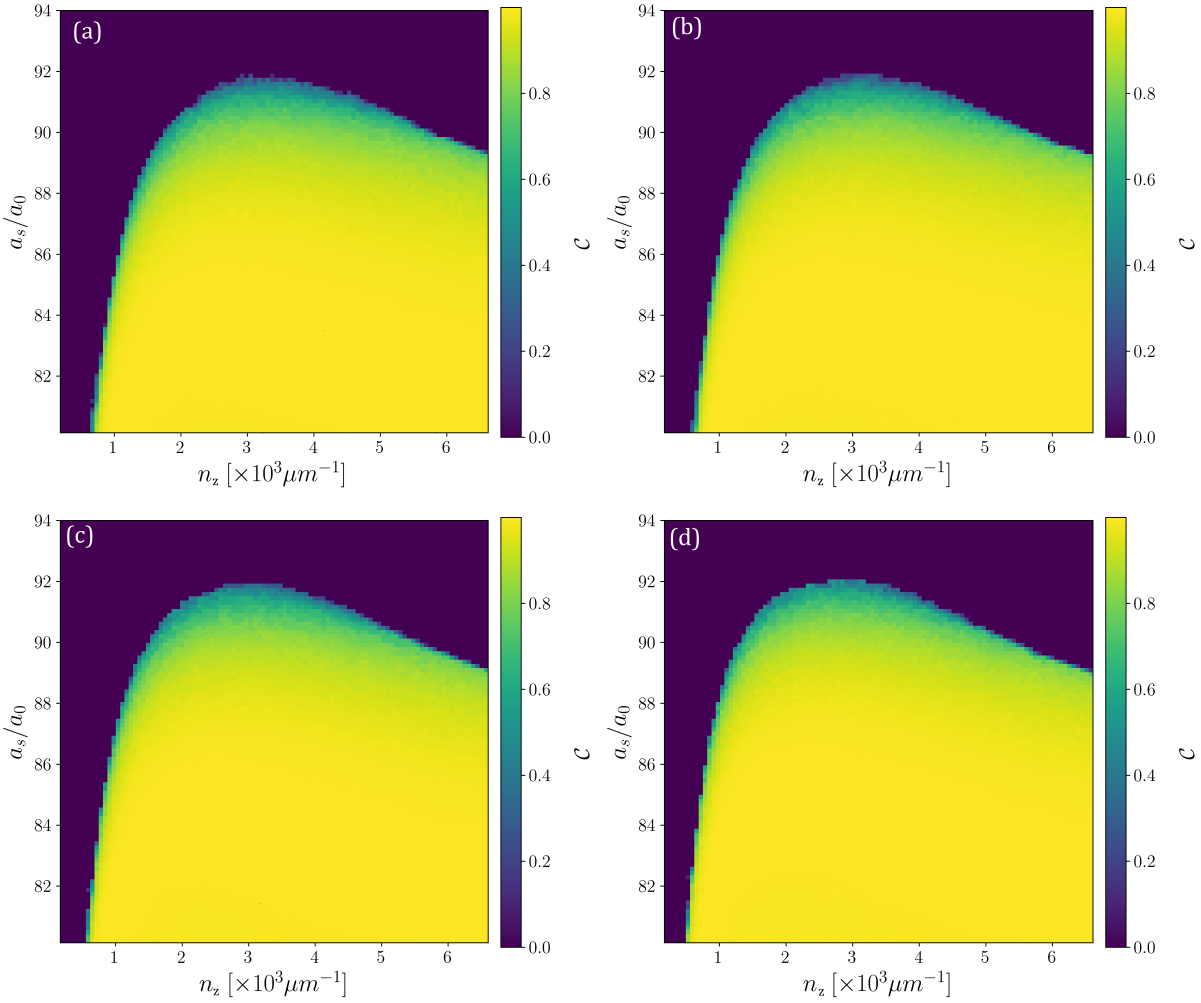

Figure 4.2: Phase diagrams displaying the contrast $\mathcal{C}$ as a function of a_s and n_z for a range of finite temperatures. a) $T = 25$ nK, b) $T = 50$ nK, c) $T = 75$ nK, d) $T = 100$ nK. Parameters are fixed to $m = m_{Dy}$ and $a_{dd} = 130.8a_0$.

heating the system drives a phase transition from a fluid into a solid phase.
Also, the superfluid region evolves towards higher a_s values and lower densities n_z as temperature increases.

We also investigate the axial density modulation as we raise the temperature. For that matter, we plot $|\Psi(z)|^2$ setting $n_z = 2.245 \times 10^3\ \mu m^{-1}$ and $a_s = 91.03a_0$ for the comparison between the $T = 0$ and $T = 50$ nK phase diagrams. For the comparison between the $T = 50$ nK and $T = 100$ nK, we investigate $n_z = 1.985 \times 10^3\ \mu m^{-1}$ and $a_s = 91.03a_0$. These points in the phase diagram are located close to the separating border between modulated states and superfluid, where the density modulation evolves as we increase the temperature. In Fig. 4.4 we depict our findings.

As expected, a phase transition is induced from modifying the temperature of the system. As we increase the temperature, the density profile becomes modulated, leading to the localization of the density in isolated droplets.

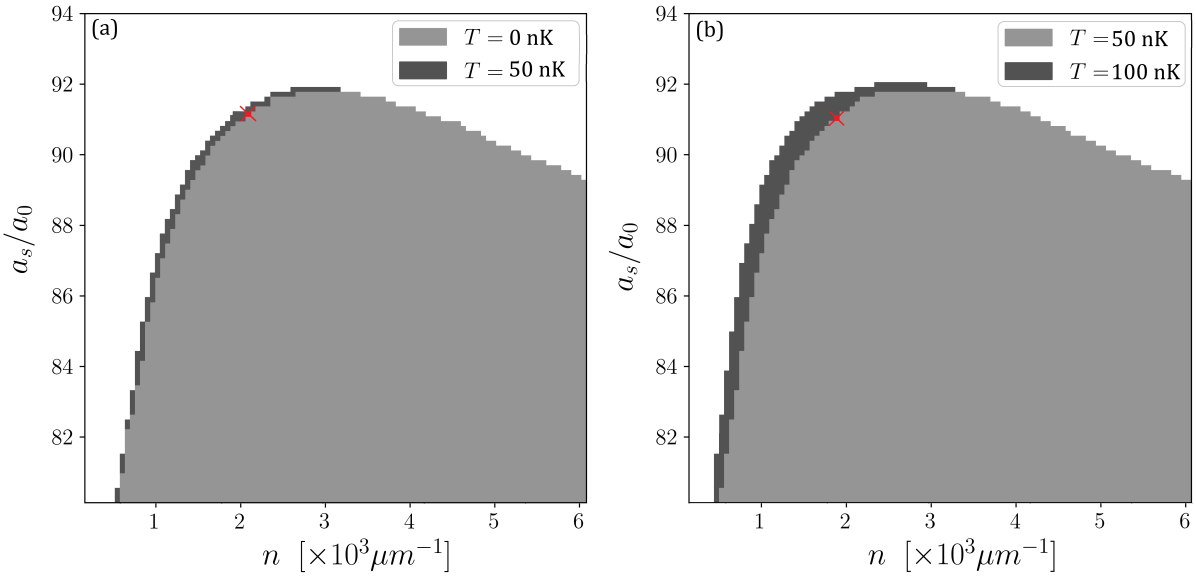

Figure 4.3: Qualitative comparison of the phase diagrams as temperature raises between (a) $T = 0$ nK and $T = 50$ nK and (b) $T = 50$ nK and $T = 100$ nK. A shift of the separating border is observed as temperature increases towards higher a_s and lower n_z. The red cross indicates the parameters employed in Fig. 4.4.

This shift in the phase diagram can be traced back to the interplay between quantum and thermal corrections as functions of the condensed density n_0. In Fig. 4.5 we depict the quantum and thermal fluctuations for the range of temperatures discussed.

Note that this result is independent of the geometry upon consideration. In Fig. 4.5, we visualize that as temperature raises, thermal corrections become more relevant as expected. However, one finds quantum fluctuations suppress large densities, such that collapse is not accessible. In contrast, as temperature is turned on, the thermal component becomes relevant and favours higher densities. In this way, the balance between these two contributions leads to the crystallization of BEC, consistent with [28]. Furthermore, thermal corrections become more important for low values of density.

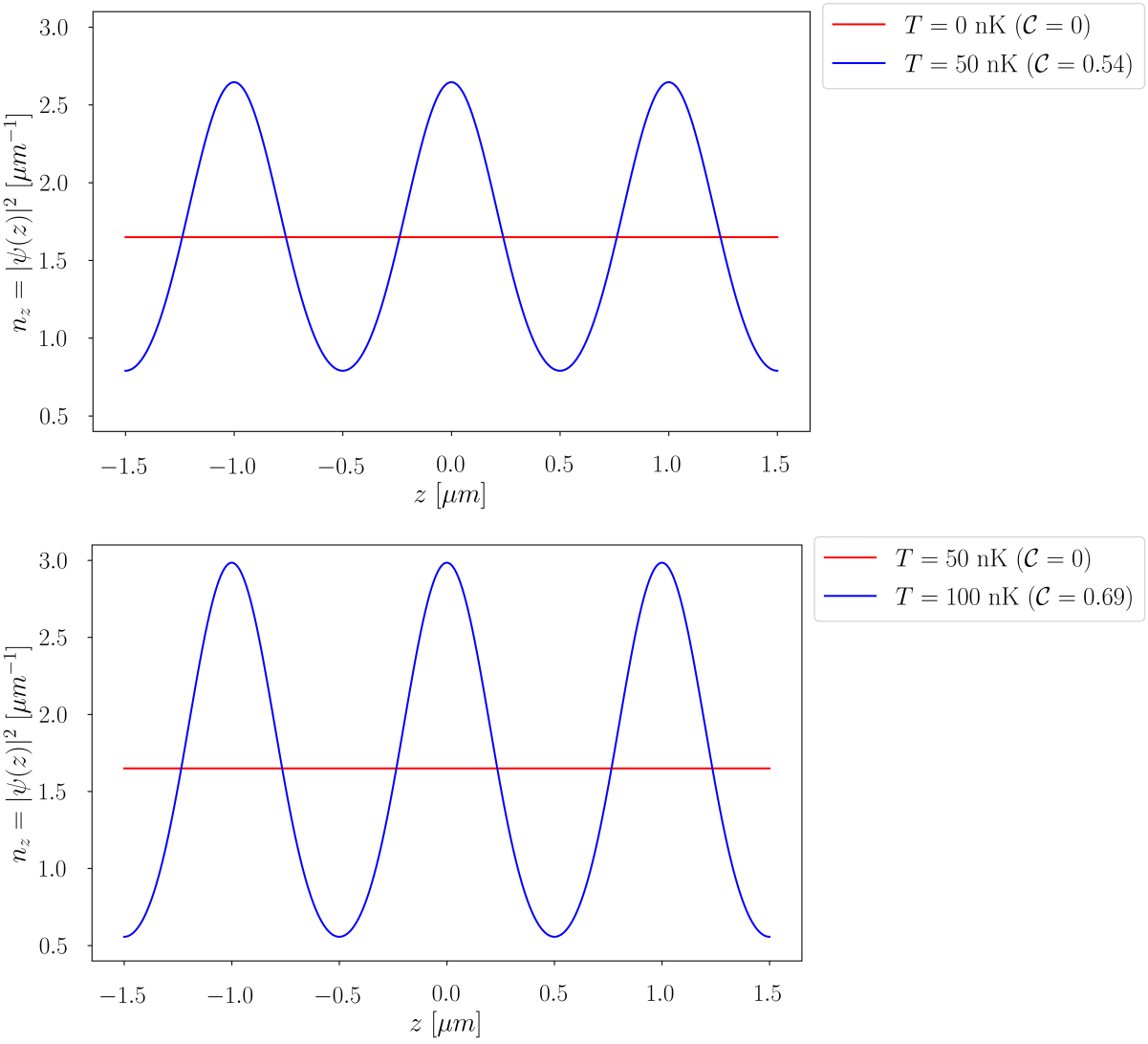

Figure 4.4: Axial density modulation along the z-axis for the droplet state due to an increase in temperature, for points localized close to the splitting border between unmodulated and modulated superfluid. We set (a) $n_z = 2.245 \times 10^3\ \mu m^{-1}$ and $a_s = 91.03 a_0$ and (b) $n_z = 1.985 \times 10^3\ \mu m^{-1}$ and $a_s = 91.03 a_0$.

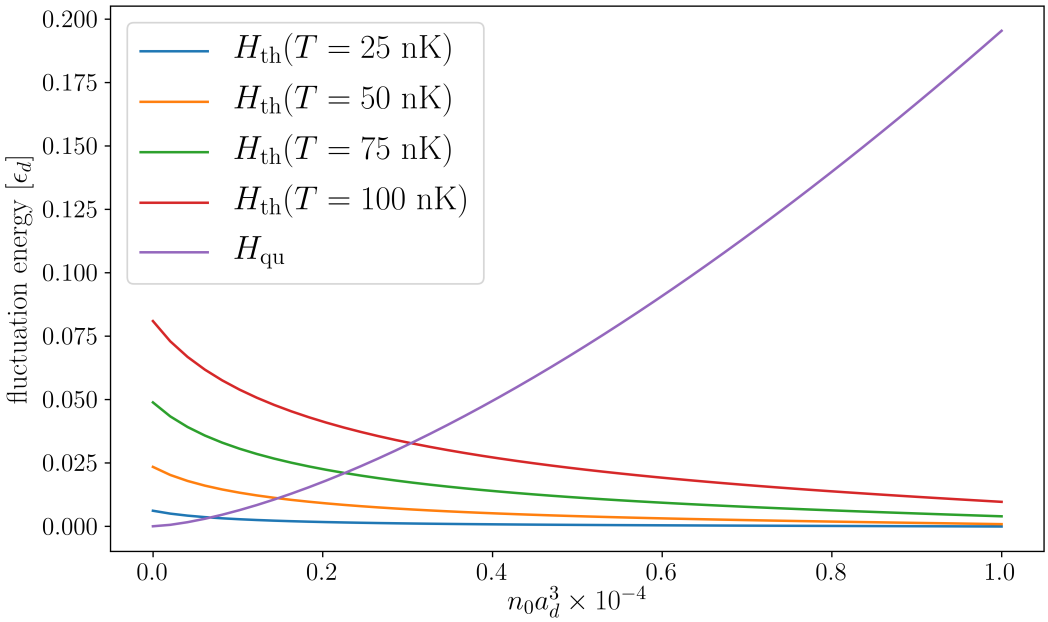

Figure 4.5: Thermal and quantum fluctuations as functions of the condensed density (equation (2.28)). As we increase the latter, the thermal fluctuation decreases while the quantum raises. Temperature is also at play, which reduces the contribution of the thermal. The fluctuation energy has been reescaled in units of $\epsilon_d = \frac{\hbar^2}{(12\pi)^2 m a_d^2}$. For the calculations we employed $a_s = 88.9 a_0 = 0.7 a_d$ and $\epsilon_{dd} = 1.46$.

Chapter 5

Conclusions

In the present work we have discussed and analyzed BEC upon the introduction of thermal fluctuations. For that matter, we have considered the general Gross-Pitaevskii equation for a dipolar BEC under a short-range (scattering) and long-range (dipole-dipole) interaction potential. Through the introduction of the Bogoliubov prescription, we find that thermal and quantum fluctuations affect the formation of localized density profiles dramatically. Therefore, the crystallization of the system is traced back to the interplay between an increasing quantum component dependent of the density and a decreasing thermal contribution, supporting the formation of regular density modulations. Consistent with [3], we approximate the temperature dependency of the corrections to a parabolic function proportional to T^2. The energy functional is therefore obtained and by introducing a simplified variational ansatz the phase diagrams for zero and finite temperatures are investigated. We find that for the zero temperature case supersolidity is accessible, consistent with [28]. We also find that, from a qualitative analysis, the order of the transition from the unmodulated density region to the quantum droplets is determined by the particle density and the scattering length, consistent with [3].
We also investigate the finite temperature phase diagrams, and find that increasing the temperature can drive a phase transition to the supersolid state. Moreover, we find this phenomenon is induced by the interplay between the beyond mean-field (quantum and thermal fluctuations) and the mean-field. Here, the quantum fluctuation opposes to higher densities while the temperature fluctuation disfavours lower densities. As a result, a balance between these two components may drive the system to the realization of BEC crystallization.

However, it should be noted that the approximations we used are coarse. For instance, we assumed that the transverse profile is Gaussian and only used a single-mode approximation in the z-direction. Furthermore, the parabolic approximation employed in the T^2 approximation for the temperature might not be sufficient for all temperatures considered. Therefore, a full numerical calculation is certainly required if one wants a quantitative precise comparison.
As an outlook one might consider employing a similar model using more than a single mode, a more appropriate transverse profile and avoid using the parabolic approximation for the temperature dependence. It is also desirable to compare the results with full numerics without approximating the thermal component upon the T^2 approximation. That could help to gain further intuition on the peculiar and fascinating physics of ultracold dipolar quantum gases.

Acknowledgements

Bartolomé Mestre would like to express his sincere gratitude to Fabian Maucher for his invaluable guidance and support throughout the research and writing process of the present work.

Chapter 6

Appendix: Supplementary information

6.1 Hartree-Fock-Bogoliubov theory

We employ the Hartree-Fock-Bogoliubov factorization over (2.3) in the most general case. Consequently, it generates on the second term

$$\begin{aligned}
&\left[\int d^3\mathbf{r'}\hat{\Psi}^\dagger(\mathbf{r'},t)V_{\text{int}}(\mathbf{r'}-\mathbf{r})\hat{\Psi}(\mathbf{r'},t)\right]\hat{\Psi}(\mathbf{r},t) = \\
&\left[\int d^3\mathbf{r'}(\Psi^*(\mathbf{r'})+\hat{\Phi}^\dagger(\mathbf{r'},t))V_{\text{int}}(\mathbf{r}-\mathbf{r'})(\Psi(\mathbf{r'})+\hat{\Phi}(\mathbf{r'},t))\right](\Psi(\mathbf{r})+\hat{\Phi}(\mathbf{r},t)) = \\
&\int d^3\mathbf{r}\Psi^*(\mathbf{r'})V_{\text{int}}(\mathbf{r}-\mathbf{r'})\Psi(\mathbf{r'})\Psi(\mathbf{r}) + \int d^3\mathbf{r}\hat{\Phi}^\dagger(\mathbf{r'},t)V_{\text{int}}(\mathbf{r}-\mathbf{r'})\hat{\Phi}(\mathbf{r'},t)\Psi(\mathbf{r})+ \\
&\int d^3\mathbf{r}\hat{\Phi}^\dagger(\mathbf{r'},t)V_{\text{int}}(\mathbf{r}-\mathbf{r'})\Psi(\mathbf{r'})\Psi(\mathbf{r}) + \int d^3\mathbf{r}\Psi^*(\mathbf{r'})V_{\text{int}}(\mathbf{r}-\mathbf{r'})\hat{\Phi}(\mathbf{r'},t)\Psi(\mathbf{r})+ \\
&\int d^3\mathbf{r}\Psi^*(\mathbf{r'})V_{\text{int}}(\mathbf{r}-\mathbf{r'})\Psi(\mathbf{r'})\hat{\Phi}(\mathbf{r},t) + \int d^3\mathbf{r}\hat{\Phi}^\dagger(\mathbf{r'},t)V_{\text{int}}(\mathbf{r}-\mathbf{r'})\hat{\Phi}(\mathbf{r'},t)\hat{\Phi}(\mathbf{r},t)+ \\
&\int d^3\mathbf{r}\hat{\Phi}^\dagger(\mathbf{r'},t)V_{\text{int}}(\mathbf{r}-\mathbf{r'})\Psi(\mathbf{r'})\hat{\Phi}(\mathbf{r},t) + \int d^3\mathbf{r}\Psi^*(\mathbf{r'})V_{\text{int}}(\mathbf{r}-\mathbf{r'})\hat{\Phi}(\mathbf{r'},t)\hat{\Phi}(\mathbf{r},t)
\end{aligned} \tag{6.1}$$

We then take the average over the previous equation. By neglecting terms of the third order, only four terms do not vanish

$$\begin{aligned}
&\left\langle\left[\int d^3\mathbf{r'}\hat{\Psi}^\dagger(\mathbf{r'},t)V_{\text{int}}(\mathbf{r}-\mathbf{r'})\hat{\Psi}(\mathbf{r'},t)\right]\hat{\Psi}(\mathbf{r},t)\right\rangle = \\
&\int d^3\mathbf{r}V_{\text{int}}(\mathbf{r}-\mathbf{r'})|\Psi(\mathbf{r'})|^2\Psi(\mathbf{r}) + \int d^3\mathbf{r}V_{\text{int}}(\mathbf{r}-\mathbf{r'})\tilde{n}(\mathbf{r'})\Psi(\mathbf{r})+ \\
&\int d^3\mathbf{r}V_{\text{int}}(\mathbf{r}-\mathbf{r'})\tilde{n}(\mathbf{r'},\mathbf{r})\Psi(\mathbf{r'}) + \int d^3\mathbf{r}V_{\text{int}}(\mathbf{r}-\mathbf{r'})\tilde{m}(\mathbf{r'},\mathbf{r})\Psi^*(\mathbf{r'})
\end{aligned} \tag{6.2}$$

Equation (**??**) has been employed to express the result in terms of $\tilde{n}$ and $\tilde{m}$. First two terms are included in the definition of $\mathcal{L}$ in (2.6), and the last two are found in (2.5).

Furthermore, equations displayed in (2.12) has been obtained from

$$\begin{aligned}
\tilde{n}(\mathbf{r}) &= \langle\hat{\Phi}^\dagger(\mathbf{r},t)\hat{\Phi}(\mathbf{r},t)\rangle \\
&= \langle\sum_\nu u_\nu^*(\mathbf{r})\hat{a}_\nu^\dagger u_\nu(\mathbf{r})\hat{a}_\nu + v_\nu^*(\mathbf{r})\hat{a}_\nu v_\nu(\mathbf{r})\hat{a}_\nu^\dagger + u_\nu(\mathbf{r})v_\nu(\mathbf{r})\hat{a}_\nu\hat{a}_\nu e^{\frac{2iE_\nu t}{\hbar}} + u_\nu^*(\mathbf{r})v_\nu^*(\mathbf{r})\hat{a}_\nu^\dagger\hat{a}_\nu^\dagger e^{\frac{-2iE_\nu t}{\hbar}}\rangle \\
&= \sum_\nu |u_\nu(\mathbf{r})|^2\langle\hat{a}_\nu^\dagger\hat{a}_\nu\rangle + |v_\nu(\mathbf{r})|^2\langle\hat{a}_\nu\hat{a}_\nu^\dagger\rangle + u_\nu(\mathbf{r})v_\nu(\mathbf{r})\langle\hat{a}_\nu\hat{a}_\nu\rangle e^{\frac{2iE_\nu t}{\hbar}} + u_\nu^*(\mathbf{r})v_\nu^*(\mathbf{r})\langle\hat{a}_\nu^\dagger\hat{a}_\nu^\dagger\rangle e^{\frac{-2iE_\nu t}{\hbar}} \\
&= \sum_\nu \left[\left(|u_\nu(\mathbf{r})|^2 + |v_\nu(\mathbf{r})|^2\right)\langle\hat{a}_\nu^\dagger\hat{a}_\nu\rangle + |v_\nu(\mathbf{r})|^2\right]
\end{aligned} \tag{6.3}$$

where in the last step it is employed $\langle\hat{a}_\nu\hat{a}_\nu^\dagger\rangle = 1 + \langle\hat{a}_\nu^\dagger\hat{a}_\nu\rangle$ and $\langle\hat{a}_\nu\hat{a}_\nu\rangle = \langle\hat{a}_\nu^\dagger\hat{a}_\nu^\dagger\rangle = 0$.

$$\begin{aligned}
\tilde{n}(\mathbf{r'},\mathbf{r}) &= \langle\hat{\Phi}^\dagger(\mathbf{r'},t)\hat{\Phi}(\mathbf{r'},t)\rangle \\
&= \langle\sum_\nu u_\nu^*(\mathbf{r'})(\mathbf{r})\hat{a}_\nu^\dagger u_\nu(\mathbf{r})\hat{a}_\nu + v_\nu(\mathbf{r})\hat{a}_\nu v_\nu(\mathbf{r'})\hat{a}_\nu^\dagger + u_\nu(\mathbf{r})v_\nu(\mathbf{r'})\hat{a}_\nu\hat{a}_\nu e^{\frac{2iE_\nu t}{\hbar}} + u_\nu^*(\mathbf{r'})v_\nu^*(\mathbf{r})\hat{a}_\nu^\dagger\hat{a}_\nu^\dagger e^{\frac{-2iE_\nu t}{\hbar}}\rangle \\
&= \sum_\nu u_\nu^*(\mathbf{r'})u_\nu(\mathbf{r})\langle\hat{a}_\nu^\dagger\hat{a}_\nu\rangle + v_\nu^*(\mathbf{r})v_\nu^*(\mathbf{r'})\langle\hat{a}_\nu\hat{a}_\nu^\dagger\rangle + u_\nu(\mathbf{r})v_\nu(\mathbf{r'})\langle\hat{a}_\nu\hat{a}_\nu\rangle e^{\frac{2iE_\nu t}{\hbar}} + u_\nu^*(\mathbf{r'})v_\nu^*(\mathbf{r})\langle\hat{a}_\nu^\dagger\hat{a}_\nu^\dagger\rangle e^{\frac{-2iE_\nu t}{\hbar}} \\
&= \sum_\nu \left[(u_\nu^*(\mathbf{r'})u_\nu(\mathbf{r}) + v_\nu^*(\mathbf{r})v_\nu(\mathbf{r'}))\langle\hat{a}_\nu^\dagger\hat{a}_\nu\rangle + v_\nu^*(\mathbf{r})v_\nu(\mathbf{r'})\right]
\end{aligned}$$

For the anomalous density, we obtain

$$\begin{aligned}
\tilde{m}(\mathbf{r}) &= \langle\hat{\Phi}(\mathbf{r},t)\hat{\Phi}(\mathbf{r},t)\rangle \\
&= \langle\sum_\nu u_\nu(\mathbf{r})^2\hat{a}_\nu\hat{a}_\nu e^{\frac{2iE_\nu t}{\hbar}} + (v_\nu^*(\mathbf{r}))^2\hat{a}_\nu^\dagger\hat{a}_\nu^\dagger e^{\frac{-2iE_\nu t}{\hbar}} + u_\nu(\mathbf{r})v_\nu^*(\mathbf{r})\hat{a}_\nu\hat{a}_\nu^\dagger + u_\nu(\mathbf{r})v_\nu^*(\mathbf{r})\hat{a}_\nu^\dagger\hat{a}_\nu\rangle \\
&= \sum_\nu u_\nu(\mathbf{r})^2 e^{\frac{2iE_\nu t}{\hbar}} + (v_\nu^*(\mathbf{r}))^2\langle\hat{a}_\nu^\dagger\hat{a}_\nu^\dagger\rangle e^{\frac{-2iE_\nu t}{\hbar}} + u_\nu(\mathbf{r})v_\nu^*(\mathbf{r})\langle\hat{a}_\nu\hat{a}_\nu^\dagger\rangle + u_\nu(\mathbf{r})v_\nu^*(\mathbf{r})\langle\hat{a}_\nu^\dagger\hat{a}_\nu\rangle \\
&= \sum_\nu \left[2u_\nu(\mathbf{r})v_\nu^*(\mathbf{r})\langle\hat{a}_\nu\hat{a}_\nu^\dagger\rangle + u_\nu(\mathbf{r})v_\nu^*(\mathbf{r})\right]
\end{aligned} \tag{6.4}$$

$$\begin{aligned}
\tilde{m}(\mathbf{r'},\mathbf{r}) &= \langle\hat{\Phi}(\mathbf{r'},t)\hat{\Phi}(\mathbf{r},t)\rangle \\
&= \langle\sum_\nu u_\nu(\mathbf{r'})u_\nu(\mathbf{r})\hat{a}_\nu\hat{a}_\nu e^{\frac{2iE_\nu t}{\hbar}} + v_\nu^*(\mathbf{r'})v_\nu^*(\mathbf{r})\hat{a}_\nu^\dagger\hat{a}_\nu^\dagger e^{\frac{-2iE_\nu t}{\hbar}} + u_\nu(\mathbf{r'})v_\nu^*(\mathbf{r})\hat{a}_\nu\hat{a}_\nu^\dagger + u_\nu(\mathbf{r})v_\nu^*(\mathbf{r'})\hat{a}_\nu^\dagger\hat{a}_\nu\rangle \\
&= -\sum_\nu u_\nu(\mathbf{r'})u_\nu(\mathbf{r})\langle\hat{a}_\nu\hat{a}_\nu\rangle e^{\frac{2iE_\nu t}{\hbar}} + v_\nu^*(\mathbf{r'})v_\nu^*(\mathbf{r})\langle\hat{a}_\nu^\dagger\hat{a}_\nu^\dagger\rangle e^{\frac{-2iE_\nu t}{\hbar}} + u_\nu(\mathbf{r'})v_\nu^*(\mathbf{r})\langle\hat{a}_\nu\hat{a}_\nu^\dagger\rangle + u_\nu(\mathbf{r})v_\nu^*(\mathbf{r'})\langle\hat{a}_\nu^\dagger\hat{a}_\nu\rangle \\
&= -\sum_\nu \left[(u_\nu(\mathbf{r'})v_\nu^*(\mathbf{r}) + u_\nu(\mathbf{r})v_\nu^*(\mathbf{r'}))\langle\hat{a}_\nu\hat{a}_\nu^\dagger\rangle + u_\nu(\mathbf{r})v_\nu^*(\mathbf{r'})\right]
\end{aligned} \tag{6.5}$$

6.2 Thermal and quantum corrections

We aim to derive (2.27) from (2.25) by employing $d^3\mathbf{k} = k^2 sin(\vartheta)dkd\vartheta d\phi$ in spherical coordinates. Also, equations displayed in (2.16) are obtained from (2.16) by using the ansatz discussed below. ϕ is constrained to $[0, 2\pi]$, thus the ϕ integral yields 2π (no dependency with ϕ). Moreover, by using $u = \cos(\vartheta)$ it is generated $du = -\sin(\vartheta)d\vartheta$, such that $d^3\mathbf{k} = -dkdu$. Note that ϑ is constrained to $[0, \pi]$, hence $u \in [-1, 1]$. In addition, we employ the variable change $k = q\xi$ and therefore $dk = \frac{dq}{\xi}$. Moreover,

terms of (2.25) are rewritten as

$$\begin{aligned}
&\epsilon(\mathbf{k}) = \frac{\hbar^2 k^2}{2m} = \frac{\hbar^2 q^2}{2m\xi^2} \\
&\tilde{V}_{\text{int}} = g\left[1 + \epsilon_{dd}(3\cos^2(\vartheta) - 1)\right] = g\left[1 + \epsilon_{dd}(3u^2 - 1)\right] \\
&E(\mathbf{r}) = \sqrt{\epsilon_{\mathbf{k}}(\epsilon_{\mathbf{k}} + 2n_0(\mathbf{r})\tilde{V}_{\text{int}})} = \sqrt{\frac{\hbar^2 q^2}{2m\xi^2}(\hbar^2 q^2 2m\xi^2 + 2n_0(\mathbf{r})f(u))} = gn_0(\mathbf{r})\sqrt{q^2(q^2 + 2f(u))}
\end{aligned} \tag{6.6}$$

where we have used $\xi = \frac{\hbar}{\sqrt{2gmn_0}}$ and $f(u) = 1 + \epsilon_{dd}(3u^2 - 1)$. Therefore, $N_B(E)$ becomes

$$N_B(E(\mathbf{r})) = \frac{1}{e^{\frac{E(\mathbf{r})}{k_B T}} - 1} = \frac{1}{\exp\left[\frac{gn_0(\mathbf{r})}{k_B T}\sqrt{q^2(q^2 + 2f(u))}\right] - 1} = \frac{1}{\exp\left[\frac{\sqrt{q^2(q^2+2f(u))}}{t(\mathbf{r})}\right] - 1} \tag{6.7}$$

Hence, we insert the previous calculations in (2.25) and consider the cutoff $q \in [q_c, \infty]$, which yields

$$\begin{aligned}
\Delta\mu(\mathbf{r}) &= \int_{-1}^{1} du \int_{q_c}^{\infty} \frac{q^2 dq}{(2\pi)^2 \xi^3} g f(u) \times \left\{ \frac{\frac{\hbar^2 q^2}{2m\xi^2}}{2gn_0(\mathbf{r})\sqrt{q^2(q^2 + 2f(u))}} + \frac{n_0(\mathbf{r}) g f(u)}{2\frac{\hbar^2 q^2}{2m\xi^2}} \right. \\
&\left. -\frac{1}{2} + \frac{1}{\exp\left[\frac{\sqrt{q^2(q^2+2f(u))}}{t(\mathbf{r})}\right] - 1} \frac{\frac{\hbar^2 q^2}{2m\xi^2}}{gn_0(\mathbf{r})\sqrt{q^2(q^2 + 2f(u))}} \right\} \\
&= \frac{g}{4\pi^2 \xi^3} \int_{-1}^{1} du \int_{q_c}^{\infty} dq f(u) \times \left\{ \frac{q^2}{2\sqrt{q^2(q^2 + 2f(u))}} + \frac{f(u)}{2q^2} - \frac{1}{2} + \frac{1}{\exp\left[\frac{\sqrt{q^2(q^2+2f(u))}}{t(\mathbf{r})}\right] - 1} \right. \\
&\left. \times \frac{q^2}{\sqrt{q^2(q^2 + 2f(u))}} \right\}
\end{aligned} \tag{6.8}$$

which is the result obtained in (2.27). Note that the $\mathbf{r}$-dependency is captured by t and ξ.
In order to describe the chemical fluctuation in a more compact form, we split (2.28) into the temperature-dependent ($\Delta\mu^{(TH)}(\mathbf{r})$) and non-temperature dependent ($\Delta\mu^{(QU)}(\mathbf{r})$) components

$$\begin{aligned}
\Delta\mu^{(TH)}(\mathbf{r}) &= \frac{g}{4\pi^2 \xi^3} \int_{-1}^{1} du \int_{q_c}^{\infty} q^2 dq f(u) \left\{ \frac{1}{\exp\left[\frac{\sqrt{q^2(q^2+2f(u))}}{t(\mathbf{r})}\right] - 1} \times \frac{q^2}{\sqrt{q^2(q^2 + 2f(u))}} \right\} \\
\Delta\mu^{(QU)}(\mathbf{r}) &= \frac{g}{4\pi^2 \xi^3} \int_{-1}^{1} du \int_{q_c}^{\infty} q^2 dq f(u) \left\{ \frac{q^2}{2\sqrt{q^2(q^2 + 2f(u))}} + \frac{f(u)}{2q^2} - \frac{1}{2} \right\}
\end{aligned} \tag{6.9}$$

Let's focus on the first. We note that it is symmetrical on u. Moreover, we apply the variable change

$q^2 \equiv Q$ such that $dQ = 2qdq = 2\sqrt{Q}dq$ and $Q \in [q_c^2, \infty]$. Therefore

$$\begin{aligned}
\Delta\mu^{(TH)}(\mathbf{r}) &= 2\frac{g}{4\pi^2\xi^3}\int_0^1 du \int_{q_c^2}^{\infty} Q\frac{dQ}{2\sqrt{Q}} f(u) \left\{ \frac{1}{\exp\left[\frac{\sqrt{Q(Q+2f(u))}}{t(\mathbf{r})}\right]-1} \times \frac{Q}{\sqrt{Q(Q+2f(u))}} \right\} \\
&= \frac{g}{4\pi^2\left(\frac{\hbar}{\sqrt{2mgn_0}}\right)^3}\int_0^1 du \int_{q_c^2}^{\infty} dQ f(u) \left\{ \frac{1}{\exp\left[\frac{\sqrt{Q(Q+2f(u))}}{t(\mathbf{r})}\right]-1} \times \frac{Q}{\sqrt{Q+2f(u)}} \right\} \\
&= \left(\frac{32}{3}g\sqrt{\frac{a_s^3}{\pi}}\right)\frac{3}{4\sqrt{2}}\int_0^1 du \int_{q_c^2}^{\infty} dQ f(u) \left\{ \frac{1}{\exp\left[\frac{\sqrt{Q(Q+2f(u))}}{t(\mathbf{r})}\right]-1} \times \frac{Q}{\sqrt{Q+2f(u)}} \right\} |\Psi(\mathbf{r})|^3
\end{aligned} \tag{6.10}$$

which is the equation showed in (2.27), where in the last step we have employed $g = \frac{4\pi\hbar^2 a_s}{m}$ and $n_0(\mathbf{r}) = |\Psi(\mathbf{r})|^2$.

For the quantum component of the local chemical potential correction, we find it is symmetrical on u as well. Therefore, we integrate over q

$$\Delta\mu^{(QU)}(\mathbf{r}) = 2\frac{g}{4\pi^2\xi^3}\int_0^1 du \frac{f(u)\left(\sqrt{8f(u)+4q_c^2}(16f(u)-4q_c^2) - 24q_c f(u) + 8q_c^3\right)}{48} \tag{6.11}$$

Manipulating (6.11) it produces

$$\begin{aligned}
\Delta\mu^{(QU)}(\mathbf{r}) &= 2\frac{g}{4\pi^2\xi^3}\int_0^1 du f(u)\frac{\sqrt{2f(u)+q_c^2}(4f(u)-q_c^2) - 3f(u)q_c + q_c^3}{6} \\
&= 2\frac{g}{4\pi^2\xi^3}\int_0^1 du f(u)\frac{\sqrt{2f(u)+q_c^2}(4f(u)-q_c^2) - 3f(u)q_c + q_c^3}{6} \\
&= \left(\frac{32}{3}g\sqrt{\frac{a_s^3}{\pi}}\right)\frac{1}{4\sqrt{2}}\int_0^1 du f(u)\left[(4f(u)-q_c^2)\sqrt{2f(u)+q_c^2} - 3f(u)q_c + q_c^3\right]|\Psi(\mathbf{r})|^3
\end{aligned} \tag{6.12}$$

as obtained in (2.28).

For the derivation of (2.30) and (2.31) we shall follow analog steps as the realized in the previous calculation of $\Delta\mu$.

Finally, in order to demonstrate (2.35), let's take the functional derivative over the previous equation. If the first is well written, we expect to obtain (2.34). In this way, we calculate the functional derivative

of each term of (2.35)

$$
\begin{aligned}
&\frac{\delta}{\delta\Psi^*(\mathbf{r})}\left[\int d^3\mathbf{r}\Psi^*(\mathbf{r})\left[-\frac{\hbar^2}{2m}\nabla^2+V_{\text{ext}}(\mathbf{r})\right]\Psi(\mathbf{r})\right]=\left[-\frac{\hbar^2}{2m}\nabla^2+V_{\text{int}}(\mathbf{r})\right]\Psi(\mathbf{r})\\
&\frac{\delta}{\delta\Psi^*(\mathbf{r})}\left[\frac{1}{2}\int d^3\mathbf{r}\int d^3\mathbf{r'}[\Psi^*(\mathbf{r})\Psi(\mathbf{r})]V_{\text{int}}(\mathbf{r}-\mathbf{r'})|\Psi(\mathbf{r'})|^2\right]=\int d^3\mathbf{r'}V_{\text{ext}}(\mathbf{r}-\mathbf{r'})|\Psi(\mathbf{r'})|^2\Psi(\mathbf{r})\\
&\frac{\delta}{\delta\Psi^*(\mathbf{r})}\left[\frac{2}{5}\int d^3\mathbf{r}\gamma[\Psi^*(\mathbf{r})\Psi(\mathbf{r})]^{\frac{5}{2}}\right]=\gamma\Psi(\mathbf{r})^{\frac{5}{2}}\Psi^*(\mathbf{r})^{\frac{3}{2}}=\gamma|\Psi(\mathbf{r})|^3\Psi(\mathbf{r})\\
&\frac{\delta}{\delta\Psi^*(\mathbf{r})}\left[2\int d^3\mathbf{r}\Theta T^2\sqrt{\Psi^*(\mathbf{r})\Psi(\mathbf{r})}\right]=\Theta T^2\frac{\sqrt{\Psi(\mathbf{r})}}{\sqrt{\Psi^*(\mathbf{r})}}=\Theta T^2\frac{\Psi(\mathbf{r})}{|\Psi(\mathbf{r})|}\\
&\frac{\delta}{\delta\Psi^*(\mathbf{r})}\left[N\mu\right]=\mu\Psi(\mathbf{r})
\end{aligned}
\tag{6.13}
$$

which are the terms displayed in (2.34).

Bibliography

[1] A. Einstein. Quantentheoric des einatomigen idealen Gases. *Preussische Akademie der Wissenshaften*, 22:261, 1924.

[2] K. Aikawa, A. Frisch, M. Mark, S. Baier, A. Rietzler, R. Grimm, and F. Ferlaino. Bose-Einstein Condensation of Erbium. *Phys. Rev. Lett.*, 108:210401, 2012.

[3] E. Aybar and M. Ö. Oktel. Temperature-dependent density profiles of dipolar droplets. *Phys. Rev. A*, 99:013620, 2019.

[4] Weizhu Bao, Yongyong Cai, and Hanquan Wang. Efficient numerical methods for computing ground states and dynamics of dipolar Bose–Einstein condensates. *Journal of Computational Physics*, 229(20):7874–7892, 2010.

[5] R. N. Bisset, R. M. Wilson, D. Baillie, and P. B. Blakie. Ground-state phase diagram of a dipolar condensate with quantum fluctuations. *Phys. Rev. A*, 94:033619, 2016.

[6] P. B. Blakie, D. Baillie, L. Chomaz, and F. Ferlaino. Supersolidity in an elongated dipolar condensate. *Phys. Rev. Res.*, 2:043318, 2020.

[7] Tim Byrnes, Daniel Rosseau, Megha Khosla, Alexey Pyrkov, Andreas Thomasen, Tetsuya Mukai, Shinsuke Koyama, Ahmed Abdelrahman, and Ebubechukwu Ilo-Okeke. Macroscopic quantum information processing using spin coherent states. *Optics Communications*, 337:102–109, 2015. Macroscopic quantumness: theory and applications in optical sciences.

[8] Tim Byrnes, Kai Wen, and Yoshihisa Yamamoto. Macroscopic quantum computation using Bose-Einstein condensates. *Phys. Rev. A*, 85:040306, 2012.

[9] E. A. Cornell and C. E. Wieman. The Bose-Einstein Condensate. *Scientific American*, 278:40–45, 1998.

[10] S. Giorgini, Lev Pitaevskii, and S. Stringari. Thermodynamics of a trapped Bose-condensed gas. *Journal of Low Temperature Physics*, 109:309–355, 1997.

[11] A. Griesmaier, J. Werner, S. Hensler, J. Stuhler, and T. Pfau. Bose-Einstein Condensation of Chromium. *Phys. Rev. Lett.*, 94:160401, 2005.

[12] E P Gross. Structure of a quantized vortex in boson systems. *Il Nuovo Cimento (1955-1965)*, 20(3):454–477, 1961.

[13] Mingyang Guo, Fabian Böttcher, Jens Hertkorn, Jan-Niklas Schmidt, Matthias Wenzel, Hans Peter Büchler, Tim Langen, and Tilman Pfau. The low-energy goldstone mode in a trapped dipolar supersolid. *Nature*, 574(7778):386–389, 2019.

[14] A. Hammond, L. Lavoine, and T. Bourdel. Tunable three-body interactions in driven two-component bose-einstein condensates. *Phys. Rev. Lett.*, 128:083401, 2022.

[15] J. Hertkorn, J.-N. Schmidt, M. Guo, F. Böttcher, K. S. H. Ng, S. D. Graham, P. Uerlings, T. Langen, M. Zwierlein, and T. Pfau. Pattern formation in quantum ferrofluids: From supersolids to superglasses. *Phys. Rev. Res.*, 3:033125, 2021.

[16] H. Kadau, M. Schmitt, M. Wenzel, C. Wink, T. Maier, I. Ferrier-Barbut, and T. Pfau. Observing the Rosensweig instability of a quantum ferrofluid. *Nature*, 530(7589):194–197, 2016.

[17] W. Ketterle, D. S. Durfee, and D. M. Stamper-Kurn. Making, probing and understanding Bose-Einstein condensates. pages 67–176, 1999.

[18] P. G. Kevrekidis, D. J. Frantzeskakis, and R. Carretero-González. *Basic Mean-Field Theory for Bose-Einstein Condensates*, pages 3–21. Springer Berlin Heidelberg, Berlin, Heidelberg, 2008.

[19] T. D. Ladd, F. Jelezko, R. Laflamme, Y. Nakamura, C. Monroe, and J. L. O'Brien. Quantum computers. *Nature*, 464(7285):45–53, 2010.

[20] T. D. Lee, Kerson Huang, and C. N. Yang. Eigenvalues and eigenfunctions of a Bose system of hard spheres and its low-temperature properties. *Phys. Rev.*, 106:1135–1145, 1957.

[21] A. J. Leggett. Can a solid be "superfluid"? *Phys. Rev. Lett.*, 25:1543–1546, 1970.

[22] Aristeu Lima and Axel Pelster. Beyond mean-field low-lying excitations of dipolar Bose gases. *Physical Review A*, 86, 2011.

[23] M. Lu, N. Q. Burdick, S. H. Youn, and B. L. Lev. Strongly Dipolar Bose-Einstein Condensate of Dysprosium. *Phys. Rev. Lett.*, 107:190401, 2011.

[24] Nicholas Parker and Carlo Barenghi. *A primer on quantum fluids*. 2016. ISBN: 978-3-319-42474-3.

[25] L.P Pitaevskii. Vortex lines in an imperfect Bose gas. *Sov. Phys. JETP*, 20:451–454, 1961.

[26] Shai Ronen and John L. Bohn. Dipolar Bose-Einstein condensates at finite temperature. *Phys. Rev. A*, 76:043607, 2007.

[27] Hiroki Saito. Path-integral monte carlo study on a droplet of a dipolar Bose–Einstein condensate stabilized by quantum fluctuation. *Journal of the Physical Society of Japan*, 85(5):053001, 2016.

[28] J. Sánchez-Baena, C. Politi, F. Maucher, F. Ferlaino, and T. Pohl. Heating a dipolar quantum fluid into a solid. *Nature Communications*, 14(1):1868, 2023.

[29] S.N. Bose. Plancks Gesetz und Lichtquantenhypothese. *Zeitschrift für Physik*, 26(1):178–181, 1924.

[30] M. Sohmen, C. Politi, L. Klaus, L. Chomaz, M. J. Mark, M. A. Norcia, and F. Ferlaino. Birth, life, and death of a dipolar supersolid. *Phys. Rev. Lett.*, 126:233401, 2021.

[31] L. Tanzi, E. Lucioni, F. Famà, J. Catani, A. Fioretti, C. Gabbanini, R. N. Bisset, L. Santos, and G. Modugno. Observation of a dipolar quantum gas with metastable supersolid properties. *Phys. Rev. Lett.*, 122:130405, 2019.

[32] L. Tanzi, J. G. Maloberti, G. Biagioni, A. Fioretti, C. Gabbanini, and G. Modugno. Evidence of superfluidity in a dipolar supersolid from nonclassical rotational inertia. *Science*, 371(6534):1162–1165, 2021.

[33] Yong-Chang Zhang, Fabian Maucher, and Thomas Pohl. Supersolidity around a critical point in dipolar Bose-Einstein condensates. *Phys. Rev. Lett.*, 123:015301, 2019.